OPEN ACCESS



Self-similarities and Power Laws in the Time-resolved Spectra of GRB 190114C, GRB 130427A, GRB 160509A, and GRB 160625B

Liang Li^{1,2,3}, J. A. Rueda^{4,5,6,7}, R. Moradi^{2,4,8}, Y. Wang^{2,4,8}, S. S. Xue^{4,8}, and R. Ruffini^{2,5,6,7,8,9}

language of license of li

Abstract

Binary-driven hypernova (BdHN) models have been adopted to explain the observed properties of long gamma-ray bursts (GRBs). Here, we perform a comprehensive data analysis (temporal and spectral analysis, GeV emission, and afterglow) on GRB 130427A, GRB 160509A, and GRB 160625B. We identify three specific episodes characterized by different observational signatures and show that these episodes can be explained and predicted to occur within the framework of the BdHNe I model, as first observed in GRB 190114C and reported in an accompanying paper. Episode 1 includes the "SN-rise" with the characteristic cutoff power-law spectrum; Episode 2 is initiated by the moment of formation of the black hole, coincident with the onset of the GeV emission and the ultrarelativistic prompt emission phase, and is characterized by a cutoff power law and blackbody spectra; Episode 3 is the "cavity," with its characteristic featureless spectrum.

Unified Astronomy Thesaurus concepts: Gamma-ray bursts (629)

1. Introduction

It has been proposed that binary-driven hypernova (BdHN) models (e.g., Rueda et al. 2021, for a review) can explain the observed properties of long gamma-ray bursts (GRBs). This scheme (see Figure 1) starts at the second SN explosion in the evolutionary path of a massive binary leading to a BdHN progenitor (see, e.g., Fryer et al. 2015), namely a carbonoxygen star (CO_{core}) forming a tight (orbital period \sim 5 minutes) binary with a neutron star (NS) companion. The CO_{core} of mass $\lesssim 9-10 M_{\odot}$ undergoes core collapse, forming at its center a newborn NS (hereafter ν NS) and, at the same time, ejecting the outermost layers in a type Ic supernova (SN) explosion. The ejecta expand, and their first observational appearance is what we call the "SN-rise." The ejecta reach the NS companion, triggering a hypercritical accretion process onto it also thanks to copious neutrino-antineutrino emission (Fryer et al. 2014; Becerra et al. 2018). Numerical simulations have shown that the NS companion, by accretion, reaches the critical mass for gravitational collapse, hence forming a black hole (BH). This was first shown by two-dimensional simulations in Becerra et al. (2015) and by three-dimensional ones, first in Becerra et al. (2016) and more recently in improved smoothed-particle-hydrodynamics simulations in Becerra et al. (2019), from which the simulated images shown in Figure 1 have been taken. The fundamental contribution of these simulations has been to provide a visualization of the SN morphology that is modified from its original sphericity. A low-density region, a "cavity," is carved by the NS companion

Original content from this work may be used under the terms of the Creative Commons Attribution 4.0 licence. Any further distribution of this work must maintain attribution to the author(s) and the title of the work, journal citation and DOI.

and, once that collapses, the region is further depleted to a density as low as $\sim\!10^{-14}$ g cm $^{-3}$ by the BH formation process (see Ruffini et al. 2019b). The newborn Kerr BH, embedded in the magnetic field inherited from the collapsed NS, aligned with the BH rotation axis, and surrounded by the low-density ionized plasma of the cavity, is what forms the "inner engine" of the GRB; see Ruffini et al. (2019d) and Rueda & Ruffini (2020). The "inner engine" leads to MeV emission due to the e^+e^- plasma created by vacuum polarization in the ultrarelativistic prompt emission (UPE) and to GeV emission by the synchrotron emission of accelerated electrons moving in the magnetic field. Details of these quantum and classical electrodynamics processes driven by the "inner engine" are given in companion papers (Moradi et al. 2021; Ruffini et al. 2021). The portion of the e^+e^- plasma that enters the highdensity region of the ejecta produces X-ray flares observed in the early afterglow (Ruffini et al. 2018d). The synchrotron emission by relativistic particles injected from the νNS into the expanding ejecta in the νNS magnetic field explains the X-ray afterglow and its power-law luminosity (Ruffini et al. 2018c; Wang et al. 2019b). Finally, the optical emission from the ejecta due to the traditional nickel decay is observed in the optical bands a few days after the GRB trigger.

On 2019 January 15, we indicated that GRB 190114C, discovered by the Fermi Gamma-ray Burst Monitor (GBM) on 2019 January 14 (Hamburg et al. 2019), with a redshift z=0.424 observed by the Nordic Optical Telescope (Selsing et al. 2019), had to be identified as a BdHN I due to its high isotropic total energy (Ruffini et al. 2019c). As a BdHN, we indicated that, within 18.8 ± 3.7 days, an SN should be expected to appear in the same location as the GRB. After an extended campaign involving tens of observatories worldwide, the expected optical SN signal was confirmed (Melandri et al. 2019). This success and the

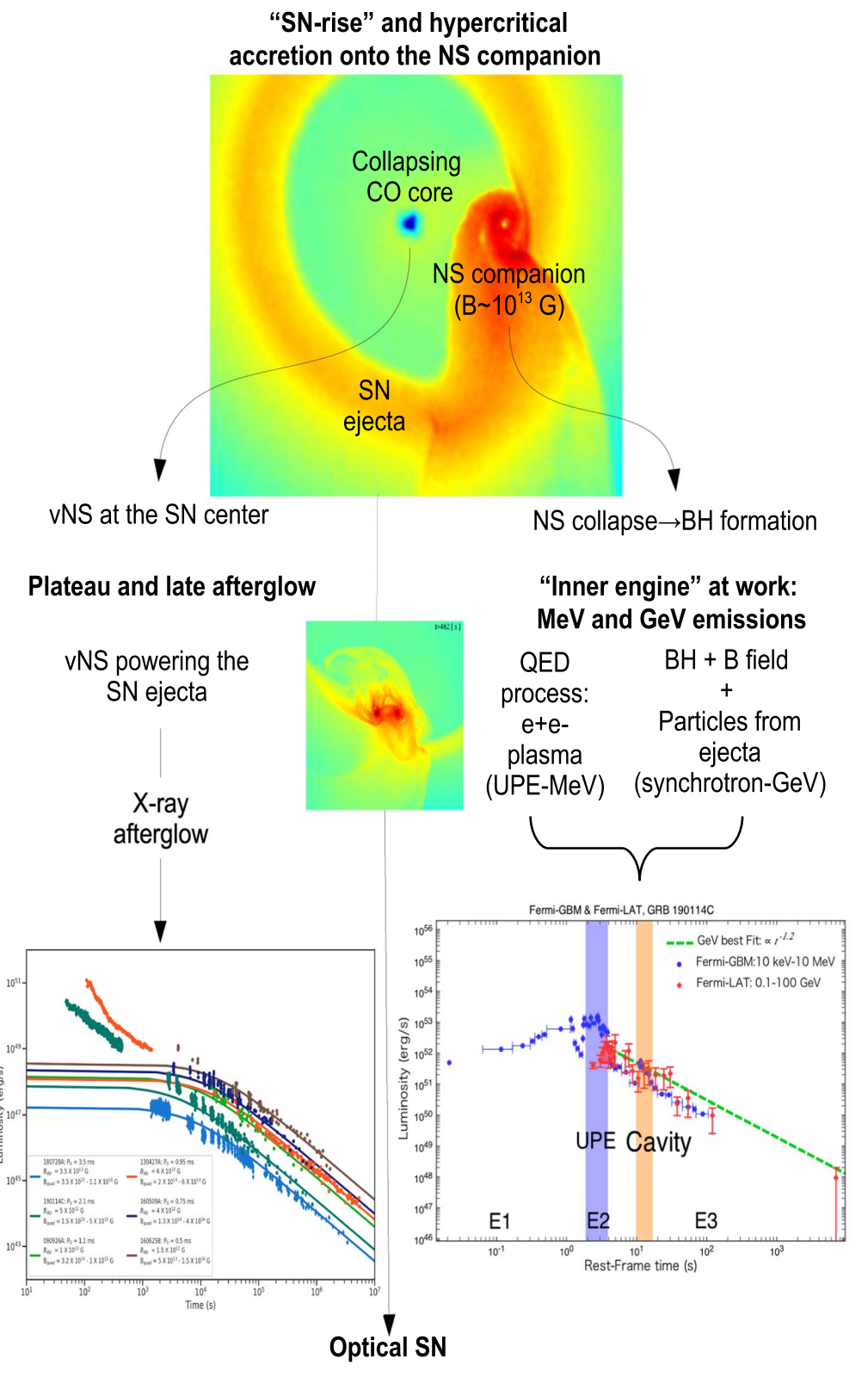


Figure 1. A diagram showing a BdHN's evolutionary history, including binary evolution, SN explosion, NS accretion, BH formation, GRB prompt and afterglow emissions, and SN appearance (see also Rueda et al. 2020).

detection of TeV radiation by MAGIC (Mirzoyan et al. 2019) make GRB 190114C one of the best examples of multi-wavelength astronomy. GRB 190114C is central for the understanding of BdHNe. For the first time all the BdHN phases are fully observable (Ruffini et al. 2019a) in a source with well

determined redshift: starting from the GBM trigger, progressing to the first appearance of the SN (the SN-rise), to the accretion of the SN ejecta in the companion neutron star (NS), to the moment of formation of the BH and the concomitant onset of the GeV emission, the discovery of self-similarities in the GBM emission

(the UPE phase), the X-ray emission from the cavity (Ruffini et al. 2019b), the emission of the afterglow (Rueda et al. 2020), the late emission of the GeV and TeV radiation and the determination of the BH mass (Ruffini et al. 2019d), finally reaching the optical SN observations mentioned above (Melandri et al. 2019; Wang et al. 2019b). The premises have been set to reach an understanding of the nature of the TeV radiation as soon as they are published. GRB 190114C signals a profound change of paradigm in the traditional understanding of GRBs from both an observational and a theoretical point of view.

It has been well established that all GRBs can be subdivided into nine subclasses of binary systems, each composed of a different combination of white dwarfs (WDs), carbon-oxygen cores (CO_{core}), NSs, and BHs (see, e.g., Wang et al. 2019a, and references therein). The most numerous subclass are BdHNe with progenitor binary systems composed of a CO_{core}, undergoing an SN explosion in the presence of an NS or BH companion (Ruffini et al. 2018d). A subclass of BdHN is represented by BdHNe I, sources with a binary period as short as \sim 4–5 minutes, where the hypercritical accretion of the SN onto the companion NS leads it to reach the critical mass for gravitational collapse, and so to form a BH. GRB 190114C is the first complete example of a BdHN I. A second subclass is represented by BdHNe II, sources with a longer binary period/ larger separation, where the hypercritical accretion of the SN onto the NS companion is not sufficient to reach the critical mass. In both BdHNe I and II the trigger of the GRB is signaled by the SN event, which leads to the formation of a new NS (ν NS), to the appearance of the SN-rise, and to the consequent hypercritical accretion on both the companion NS and the ν NS. By proceeding with an unprecedented spectral analysis in ever decreasing time steps, we have discovered self-similarities in the GBM emission of the UPE phase; see Ruffini et al. (2019a). There, we have addressed the nature of the "inner engine" of BdHNe creating the structure of self-similarity: a Kerr BH embedded in a magnetic field aligned with its rotation axis and surrounded a very low-density electron-ion plasma (Ruffini et al. 2019b). We have shown that the extraction of energy from the BH leads to the discrete and quantized MeV and GeV radiation, as presented in the companion papers (Ruffini et al. 2019a, 2019d; Rueda & Ruffini 2020).

The main purpose of this article is to verity that the results obtained in GRB 190114C are not an isolated case; on the contrary, they are verified to exist to an equal level of confidence in the other BdHNe I: GRB 130427A, GRB 160509A, and GRB 160625B. In all these sources, starting from the GBM trigger and a well determined redshift, we have progressed to identify: in Episode 1, the precursor including the first appearance of the SN (the "SN-rise") and the accretion of the SN ejecta onto the companion NS; in Episode 2, the moment of formation of the BH, the simultaneous onset of the GeV emission, and the onset of the UPE phase with its characteristic cutoff power law plus blackbody spectra observed by Fermi; in Episode 3, the X-ray emission from the "cavity" recently modeled in Ruffini et al. (2019b). GRB 130427A is characterized by its extremely high fluence in MeV and GeV emission (Maselli et al. 2014; Ruffini et al. 2015). GRB 160509A is found to have a significant GeV evolution (Tam et al. 2017). GRB 160625B is famous for the confident detection of polarization (Troja et al. 2017). The data analysis in these papers confirms the existence of three light-curve structures in the initial tens of seconds, and in this paper we

perform a more detailed analysis and give the astrophysical interpretations, categorizing the three light-curve structures as (1) SN-rise (Ruffini et al. 2019a), (2) UPE phase (Ruffini et al. 2019a), and (3) transition from SN to hypernova (Ruffini et al. 2018b). Particular attention is given to the accuracy of the spectral analysis to identify the above three episodes, as well as the much more complex iterative statistical analysis on the UPE to identify the self-similarities and the associated power laws. The fact that in all these cases the results have been successful implies that we have made great progress in ascertaining the taxonomy of a standard BdHN I. We are also going to show an example of BdHN II to compare and contrast the results. It is by now clear that the research is open in two different directions: in deepening the nature of each single component of a BdHN I, by inserting it into a population synthesis analysis (see, e.g., discussion in Fryer et al. 2015), and in studying the microphysical and physical origin of the self-similarities and the associated power laws.

As pointed out in the well documented book by Zhang (2018), the traditional approach in the spectroscopic data analysis of BATSE on board the Compton Gamma-Ray Observatory (Preece et al. 2000) has typically addressed a time-integrated spectral analysis over the entire duration of T_{90} and the finding of commonalities in all GRBs. This approach has been continued all the way to the current Fermi-GBM observations and the observations of the BAT instrument on board the Neil Gehrels Swift Observatory (see, e.g., Abdo et al. 2009; Hamburg et al. 2019, by the Fermi team). The timeintegrated spectrum has been traditionally fitted by a smoothly connected, broken power-law function, named the "Band" function (Band et al. 1993). The Band function is based on four parameters $(A, \alpha, \beta, \text{ and } E_p)$ whose values vary from source to source without reaching universal values. A complementary spectral analysis limited to the brightest time bin has been addressed by fitting with power laws, smoothly broken power laws, and Comptonized and Band models (Gruber et al. 2014). On the other hand, GRBs are known to have strong spectral evolution (e.g., Lu et al. 2012; Guiriec et al. 2013, 2015b; Li 2019a; Yu et al. 2019; Li et al. 2021). Therefore, in order to study their potential radiation mechanism in great detail, a time-resolved spectral analysis approach is required. The timeresolved spectral analysis has been performed for some bright bursts by some authors, e.g., GRB 090618, GRB 130427A, GRB 190114C, and many others (e.g., Ryde 2004, 2005; Izzo et al. 2012; Ruffini et al. 2014, 2015, 2019a).

The Fermi satellite, launched in 2008, provides a wider observational window in energy (Fermi-GBM: 8 keV-40 MeV, Fermi-LAT: 100 MeV-100 GeV), as well as a higher time resolution (as low as 2 μ s for time-tagged event data; see, e.g., Meegan et al. 2009; von Kienlin et al. 2014). Gruber et al. (2014) presented the catalog of spectral analyses of GRBs by Fermi-GBM during its first four years of operation. Their aim was to generalize the statistical properties from the observations, not to differentiate the processes occurring in different episodes. They studied two types of spectra: the time-integrated spectrum and the spectrum of the brightest time bin. The software of RMfit (version 4.0rcl) was employed, which applies a modified, forward-folding Levenberg-Marquardt algorithm for spectral fitting. Four different spectral models were adopted: Band, Comptonized cutoff power law (CPL), power law (PL), and smoothly broken power law (SBPL). For the fitting results of the time-integrated spectra, they found the

fractions of the best model from the statistical results are 29.9%, 6.6%, 8.6%, and 54.7% for PL, SBPL, Band, and CPL, respectively. For the fitting results of the brightest time bin, they found the fractions of the best model from the statistical results are 54.4%, 1.9%, 2.6%, and 39.7% for PL, SBPL, Band, and CPL, respectively. The Band and SBPL models are not preferred for most GRBs. The PL and CPL models are preferred for most GRBs; the popularity of the simple PL model was interpreted as an observational effect. In our approach since 2018, we have used the data from the Neil Gehrels Swift and Fermi satellites; our priority of having bright GRBs has already been stated in the introduction. The reason why these four different models are adopted is that the measurable spectrum of GRBs is dependent on intensity, and less intense bursts provide fewer data to support a large number of parameters. This may appear obvious, but it allows us to determine why in many situations a particular empirical function provides a poor fit, while in other cases it provides an accurate fit. For example, the energy spectra of GRBs are normally well fit by two smoothly joined power laws. For particularly bright GRBs, the Band and SBPL functions are typically an accurate description of the spectrum, while for weaker bursts the Comptonized function is most appropriate. Bursts that have signal significance of the order of the background fluctuations do not have a detectable distinctive break in their spectrum and so the power law is the most appropriate function. These facts reflect that in order to affirm the reliable physical interpretation from the spectra, both the quality and quantity of the observed data are important. In other words, capable satellites and bright GRBs are required. In this article, our sample consists of bright GRBs, which are well observed by both Fermi-GBM and Fermi-LAT. For these GRBs, Fermi is able to distinguish, for a small time interval (e.g., 0.1 s), the best model from two or more given models; therefore, a time-resolved spectral analysis can confidently be performed. In practice, we consider that an entire GRB phenomenon is composed of many episodes. We analyze the time-resolved spectral evolution and check that the goodness of the data is able to differentiate the episodes occurring at different times, including precursor, SN-rise, UPE, cavity, afterglow, and GeV emission. Consequently, from the composition of different episodes in each GRB, the taxonomy of nine subclasses of GRBs is obtained.

Therefore, we have correspondingly defined our priorities: (1) to address only the brightest GRBs observed by Fermi-GBM, Fermi-LAT, and the Neil Gehrels Swift Observatory, so addressing a limited number of sources with high significance S and in a wider range of spectral energies; (2) in view of the strongest significance S, to identify episodes that present specific spectral structures and determine the duration ΔT of each episode in the source rest frame; (3) to perform a detailed time-resolved spectral analysis on ever decreasing time intervals, within the total duration ΔT , which has led to identification of the presence of self-similar structures and associated power laws. We have determined new statistically significant spectral distributions and evaluated the corresponding luminosity in the cosmological rest frame.

The structure of this article is as follows. Section 2 presents the detailed time-resolved data analysis procedure. We have fully considered the spectral contribution from thermal components. Our approach to the spectral analysis is based on fitting Bayesian models by using the Markov Chain Monte

Carlo (MCMC) technique. In Section 3, we derive our complete spectral analysis for all the episodes of GRB 160625B. In Section 4, we derive the complete spectral analysis for GRB 160509A. In Section 5, we present the corresponding analysis for GRB 130427A, which is the only case in which the UPE analysis is hampered by the pileup problem. In Section 6, we recall the result of the BdHNe II GRB 180728A. In Section 7, we summarize the results on the analysis of the SN-rise of BdHNe I and II, and present the implications of these results in the physical and astrophysical scenario of BdHNe. In Section 8, we draw the general conclusions of this work.

2. Data Analysis

2.1. Spectral Analysis

The temporal and spectral analysis of Fermi-GBM data is performed using the Bayesian approach package, namely, the Multi-Mission Maximum Likelihood Framework (3ML, Vianello et al. 2015). The GBM (Meegan et al. 2009) carries 14 detectors: 12 sodium iodide (NaI, 8 keV-1 MeV) and two bismuth germinate (BGO, 200 keV-40 MeV) scintillation detectors. We select up to three NaI detectors and one BGO detector, the incident angles of which are less than 60° (Bhat et al. 2016). The time-tagged event and spectral response files are used for the sets of detectors selected. The pre-source and the post-source data are used to fit the background with a 0-4 order polynomial function. The time interval of the source is selected to be longer than the duration of bursts (T_{90}) , in order to cover the entire backgroundsubtracted emission. During the fitting procedure, the likelihoodbased statistics, the so-called Pgstat, is used, given by a Poisson (observation, Cash 1979)–Gaussian (background) profile likelihood. We replace the Band model by the CPL model to perform the spectral fitting throughout the paper, since thermal components are generally observed in the left shoulder of the Band spectrum (low-energy region, below $E_{\rm p}$); its existence does not affect the high-energy β index (above $E_{\rm p}$). The spectral analysis is performed by employing an MCMC technique to fit Bayesian models, and the model parameters in the Monte Carlo iteration vary in the following ranges: PL model, index: [-5, 1]; blackbody (BB) model, kT (keV): [1, 10^3]; CPL model, α : [-5, 1], E_c (keV): [1, 10⁴]. We use the typical spectral parameters from the Fermi-GBM catalog (Gruber et al. 2014) as the informative priors: $\alpha \sim \mathcal{N}(\mu = -1, \sigma = 0.5); E_c \sim \mathcal{N}(\mu = 200, \sigma = 300); \beta \sim$ $\mathcal{N}(\mu = -2.2, \sigma = 0.5)$. Each time we perform 20 chains and each chain includes 10,000 time iterations. The final value and its uncertainty (68% (1 σ) Bayesian credible level) are calculated from the last 80% of the iterations. In this paper, we adopt the deviance information criterion (DIC) to select the better of two different models, defined as DIC = $-2 \log[p(\text{data}|\hat{\theta})] + 2p_{\text{DIC}}$, where $\hat{\theta}$ is the posterior mean of the parameters and p_{DIC} is the effective number of parameters. The preferred model is the model with the lowest DIC score. We define $\Delta DIC = DIC(CPL + BB) - DIC$ (CPL); for instance, if Δ DIC is negative it indicates that the CPL + BB is better than CPL. These methods have been applied in each episode.

2.2. Spectral Models

Several basic spectral components have been proposal previously (Kaneko et al. 2006; Guiriec et al. 2010, 2011, 2015a; Zhang et al. 2011; Yu et al. 2016, 2019; Li 2019a, 2019b, 2020, 2022a, 2022b; Li et al. 2019, 2021;

Ravasio et al. 2019; Li & Zhang 2021). The observed GRB spectrum in the keV–MeV band can usually be fitted by a nonthermal component, namely, the Band (or CPL) function (Band et al. 1993). The Band function defined as

$$f_{\text{BAND}}(E) = A \begin{cases} \left(\frac{E}{E_{\text{piv}}}\right)^{\alpha} \exp(-\frac{E}{E_{0}}), & E \leqslant (\alpha - \beta)E_{0} \\ \left[\frac{(\alpha - \beta)E_{0}}{E_{\text{piv}}}\right]^{(\alpha - \beta)} \exp(\beta - \alpha) \left(\frac{E}{E_{\text{piv}}}\right)^{\beta}, & E \geqslant (\alpha - \beta)E_{0} \end{cases}$$

$$(1)$$

where

$$E_{\rm p} = (2 + \alpha)E_0,\tag{2}$$

has two power-law photon indices: the low-energy power-law photon spectral index α (typically \sim -1.0), and the high-energy power-law photon spectral index β (typically \sim -2.2), which are connected at the peak energy $E_{\rm p}$ (typically \sim 220 keV) in the νF_{ν} space (e.g., Preece et al. 2000; Kaneko et al. 2006; Li et al. 2021; Li 2022a). A is the normalization factor at 100 keV in units of photons cm⁻² keV⁻¹ s⁻¹, $E_{\rm piv}$ is the pivot energy fixed at 100 keV, and $E_{\rm 0}$ is the break energy in units of keV.

For the UPE phase, we mainly adopt the CPL model, or the so-called Comptonized model, which is given by

$$f_{\text{COMP}}(E) = A \left(\frac{E}{E_{\text{piv}}}\right)^{\alpha} e^{-E/E_0} \tag{3}$$

where A, E_{piv} , α , and E_0 are as defined above.

Some bursts have an additional thermal component and are generally fitted with a Planck BB function. The Planck function is given by

$$f_{\rm BB}(E, t) = A(t) \frac{E^2}{\exp\left[E/kT(t)\right] - 1},$$
 (4)

where A(t) is the normalization, k is the Boltzmann constant, and kT(t) is the blackbody temperature.

For the high-energy Fermi-LAT emission, the best-fit spectral model is usually a power-law model (e.g., Abdo et al. 2010; Zhang et al. 2011; Ajello et al. 2019; Tak et al. 2019) in the 0.1–100 GeV energy band, i.e.,

$$f_{\rm PL}(E) = A \left(\frac{E}{E_{\rm piv}}\right)^{\Gamma},$$
 (5)

where A is the normalization and Γ is the power-law index.

In the spectral fitting for the MeV UPE phase, we adopt a Bayesian analysis and model comparison using the ΔDIC value (e.g., Spiegelhalter et al. 2002; Moreno et al. 2013). For the GeV emission, a maximum likelihood estimate analysis is used to obtain the best fitting (e.g., Goldstein et al. 2012; Ackermann et al. 2013; Gruber et al. 2014; Bhat et al. 2016; Ajello et al. 2019; Li et al. 2019).

2.3. Calculation of Luminosity and Energetics

In addition to reporting the flux and fluence of each GRB, for the subset of GRBs with measured redshift z we also calculate their total radiated energy ($E_{\rm iso}$).

The observed flux, $\Phi(E_1, E_2, z)$, integrated between the minimum energy E_1 and the maximum energy E_2 is defined as

$$\Phi(E_1, E_2, z) = \int_{E_1/(1+z)}^{E_2/(1+z)} E f_{\text{obs}}(E) dE.$$
 (6)

In principle, for different models and different energy bands the values of E_1 , E_2 , and $f_{\rm obs}$ would be different. For instance, for GeV radiation $E_1=0.1$ GeV, $E_2=100$ GeV, and $f_{\rm obs}=f_{\rm PL}$ is obtained from Equation (5) with a typical value of $\Gamma\approx-2.5$ (Ajello et al. 2019).

We adopt a flat FLRW universe model with $\Omega_{\Lambda} = 0.714$, $\Omega_{M} = 0.286$, and $H_{0} = 69.6$ km s⁻¹ Mpc⁻¹ (Bennett et al. 2014; Planck Collaboration et al. 2016), and then the luminosity distance is given by (Weinberg 1972)

$$d_L(z, \Omega_{\Lambda}, \Omega_{M}) = (1+z)\frac{c}{H_0} \int_0^z \frac{dz'}{\sqrt{\Omega_{M}(1+z')^3 + \Omega_{\Lambda}}}.$$
 (7)

The isotropic radiated luminosity is

$$L_{\rm iso} = \frac{4\pi d_L^2}{1+z} \Phi(E_1, E_2, z), \tag{8}$$

where d_L is the luminosity distance and z is the redshift. The observed fluence S is given by

$$S(E_1, E_2, z) = \Delta T_1 \Phi(E_1, E_2, z),$$
 (9)

where ΔT_i is the duration of the time interval in which the analysis is made; see Ajello et al. (2019) for details.

The radiated energy, which is assumed to be radiated isotropically, is defined as

$$E_{\rm iso} = \frac{4\pi \ d_L^2}{1 + z} S(E_1, E_2, z). \tag{10}$$

The isotropic luminosity (L_X) for the X-ray afterglow data (Swift/XRT) can be derived as

$$L_{\text{X.iso}} = 4\pi k d_L^2 F_{\text{X.b}},\tag{11}$$

where F_X is the flux, $k = (1+z)^{\beta-1}$, and β is the spectral index, which were computed from the Swift BA + XRT repository: http://www.swift.ac.uk/burst_analyser/.

3. GRB 160625B

On 2016 June 25 at 22:40:16.28 UT, GRB 160625B triggered GBM on board the NASA Fermi Gamma-ray Space Telescope (Burns 2016). Fermi-LAT began observation 188.54 s after the trigger (Dirirsa et al. 2016), and detected more than 300 photons with energy >100 MeV; the highest photon energy was about 15 GeV (Lü et al. 2017). Swift-XRT began observation at a later time ($>10^4$ s) and found a powerlaw behavior with decaying index \sim 1.25 (Melandri et al. 2016). GRB 160625B is one of the most energetic GRBs with an isotropic energy $\approx 3 \times 10^{54}$ erg (Troja et al. 2017; Zhang et al. 2018). The redshift z = 1.406 is reported in Xu et al. (2016). GRB 160625B is a luminous GRB with clearly detected polarization (Troja 2017). There is no supernova confirmation due to its high redshift, z > 1 (Woosley & Bloom 2006). The early emission can be defined as three episodes as suggested by several independent studies in the literature (Troja et al. 2017; Zhang et al. 2018): a short precursor (G_1) , a main burst (G_2) , and a long-lasting tail (G_3) . Troja et al. (2017) detected a significant and variable linear optical polarization in G_2 , and they inferred, from the degree of

polarization of $8.3\% \pm 0.8\%$, that the GRB outflows might be dominated by Poynting flux, of which the magnetic energy is dissipated rapidly before the magnetic reconnection, producing bright gamma rays. Zhang et al. (2018) performed a meticulous time-resolved analysis and found an evolution of the thermal component in G_1 . The bright G_2 episode was divided into 71 slices, each having at least 2500 net counts, to conduct a fine time-resolved spectral analysis. All the slices can be successfully fitted by a Band function; no thermal component was determined. G_3 is faint, and its time-resolved spectra were fitted by a single power law or a cutoff power law. From the spectral evolution from thermal to nonthermal, they suggest a transition of the outflow from fireball to Poynting-flux-dominated.

Based on the temporal and spectral analysis, we confirm that the gamma-ray light curve of GRB 160625B has three different episodes, shown in Figure 2 (see also Table 1). Three different physical episodes have been identified in the keV–MeV energy range (see Figures 2, 3, and Table 1): (1) SN-rise, the time interval from $t_{\rm rf} = 0.00$ s to $t_{\rm rf} = 0.83$ s; (2) UPE phase, the time interval from $t_{\rm rf} = 77.72$ s to $t_{\rm rf} = 87.70$ s; (3) cavity, the time interval from $t_{\rm rf} = 87.70$ s to $t_{\rm rf} = 92.27$ s.

In a BdHN I, the "inner engine" starts at the moment of formation of the BH, accelerating charged particles that radiate photons in a wide energy band, thus generating the UPE phase and the GeV photons. The onset of the UPE phase is indicated by the appearance of the thermal component since the plasma is originally optically thick. Since the count rate of GeV photons observed in the onset phase is a few per second, it is necessary to have a discrepancy of at most a fraction of a second between the observed starting time of the UPE and the GeV. Indeed, for GRB 160625B, the starting time of its thermal emission is just 0.38 s ahead of the time of observation of the first GeV photon, which for the above reasons can be considered temporally coincident. This time coincidence is also observed in the other BdHNe I studied in this article.

- 1. *SN-rise*. Figure 3 (upper left panel) shows the fit of the SN-rise spectrum during its rest-frame time interval of occurrence, i.e., from 0 to $t_{\rm rf} \simeq 0.83$ s. It is best fitted by a PL + BB model with temperature 17.5 keV and power-law index -2.0.
- 2. UPE phase. Similarly to GRB 190114C, we also find a self-similarity in the UPE phase for GRB 160625B after carrying out the detailed time-resolved spectral analysis, with a cutoff power law + blackbody (CPL + BB) model, for five successive iteration processes on shorter and shorter timescales 10 (expressed in the laboratory and in the rest frame). For the first iteration, Figure 4 (first layer) shows the best fit of the spectrum of the entire duration of the UPE from $t_{\rm rf} = 77.72$ s to $t_{\rm rf} = 87.70$ s. We then divide the rest-frame time interval in half and again perform the same spectral analysis for the two intervals, each of 4.99 s, i.e., [77.72-82.71 s] and [82.71–87.70 s], obtaining the results shown in Figure 4 (second layer). In the third iteration, we divide each of these half intervals in half again. We continue this procedure up to five iterations, i.e., up to dividing the

UPE into 16 time subintervals. For each iterative step, we give the duration and the spectral parameters of the CPL + BB model, including the low-energy photon index α , the peak energy E_c , the BB temperature kT (k is the Boltzmann constant), the model comparison parameter (DIC), the BB flux, the total flux, the ratio of BB to total flux, and the total energy. The results are summarized in Figure 4 and the properties of the iterations are listed in Table 2. They confirm the validity, also in GRB 160625B, of the self-similar structure first discovered in GRB 190114C. Figure 5 shows the luminosity of the Fermi-GBM as a function of the rest-frame time, derived from the fifth iteration (see Table 2). We also show the corresponding evolution of the rest-frame temperature (Figure 5). The best-fit parameters for each spectrum (α , $E_{\rm c}$), along with its time interval, $\Delta {\rm DIC}$, blackbody temperature kT, blackbody flux (F_{BB}) , total flux (F_{total}) , ratio of thermal to total flux, and the total energy are summarized in Table 2.

- 3. *Cavity*. Figure 3 (upper right panel) shows the spectrum of the cavity for GRB 160625B, from $t_{\rm rf} = 87.70 \, {\rm s}$ to $t_{\rm rf} = 92.27 \, {\rm s}$. It can be well fitted by a featureless CPL model with photon index $\alpha = 0.95$ and cutoff energy of 239 keV.
- 4. *GeV emission*. Figure 3 (lower left panel) shows the luminosity of the GeV emission in the rest frame as a function of the rest-frame time.
- 5. Afterglow. Figure 3 (lower right panel) shows the (k-corrected) afterglow luminosity (Swift/XRT data) in the rest-frame as a function of rest-frame time. The best-fit parameters were obtained with a power-law index of 1.319 ± 0.021 .

4. GRB 160509A

GRB 160509A was observed by the Fermi satellite on 2016 May 9 at 08:59:04.36 UT (Longo et al. 2016). It was a strong source of GeV photons detected by Fermi-LAT, including a photon of 52 GeV that arrived at 77 s, and another one of 29 GeV at \sim 70 ks (Laskar et al. 2016). Swift has a late-time follow-up, with a total exposure time of 1700 s starting from 7278 s (Kangas et al. 2020). The redshift of 1.17 is measured by the Gemini North telescope (Tanvir et al. 2016), implying a high isotropic energy of 1.06×10^{54} erg (Tam et al. 2017). Pak-Hin Thomas Tam and collaborators (Tam et al. 2017) analyzed in great detail the bright multipeaked pulse from -10to 30 s, and a weaker emission period from 280 to 420 s. They divided these two episodes into six time slices, of which the Fermi-GBM and Fermi-LAT data are together fitted by a Band function or a Band function with an exponential high-energy cutoff. In Figure 6, we show the result of our highly timeresolved analysis applied to GRB 160509A, which further extends the results of Tam et al. (2017).

Based on the temporal and spectral analysis, three different physical processes are identified in the keV–MeV energy range (see Figures 6, 7, and Table 3). (1) SN-rise, the time interval from $t_{\rm rf} = 0.92$ s to $t_{\rm rf} = 1.84$ s. (2). UPE phase, the time interval from $t_{\rm rf} = 4.84$ s to $t_{\rm rf} = 8.53$ s. (3). Cavity, the time interval from $t_{\rm rf} = 10.14$ s to $t_{\rm rf} = 13.82$ s.

1. *SN-rise*. Figure 7 (upper left panel) shows the SN-rise and the spectral fitting of the cavity emission during its restframe time interval of occurrence. The spectrum of the

 $[\]overline{10}$ The "inner engine" of the BdHN extracts the rotational energy from a Kerr BH through a Wald–Papapetrou solution, located in the cavity, and a discrete emission of quanta of 10^{37} erg in a time sequence as short as 10^{-4} s, which is expected within the framework of the BdHN models. To verify this, an indepth time-resolved spectral analysis is required; for details see Ruffini et al. (2019a).

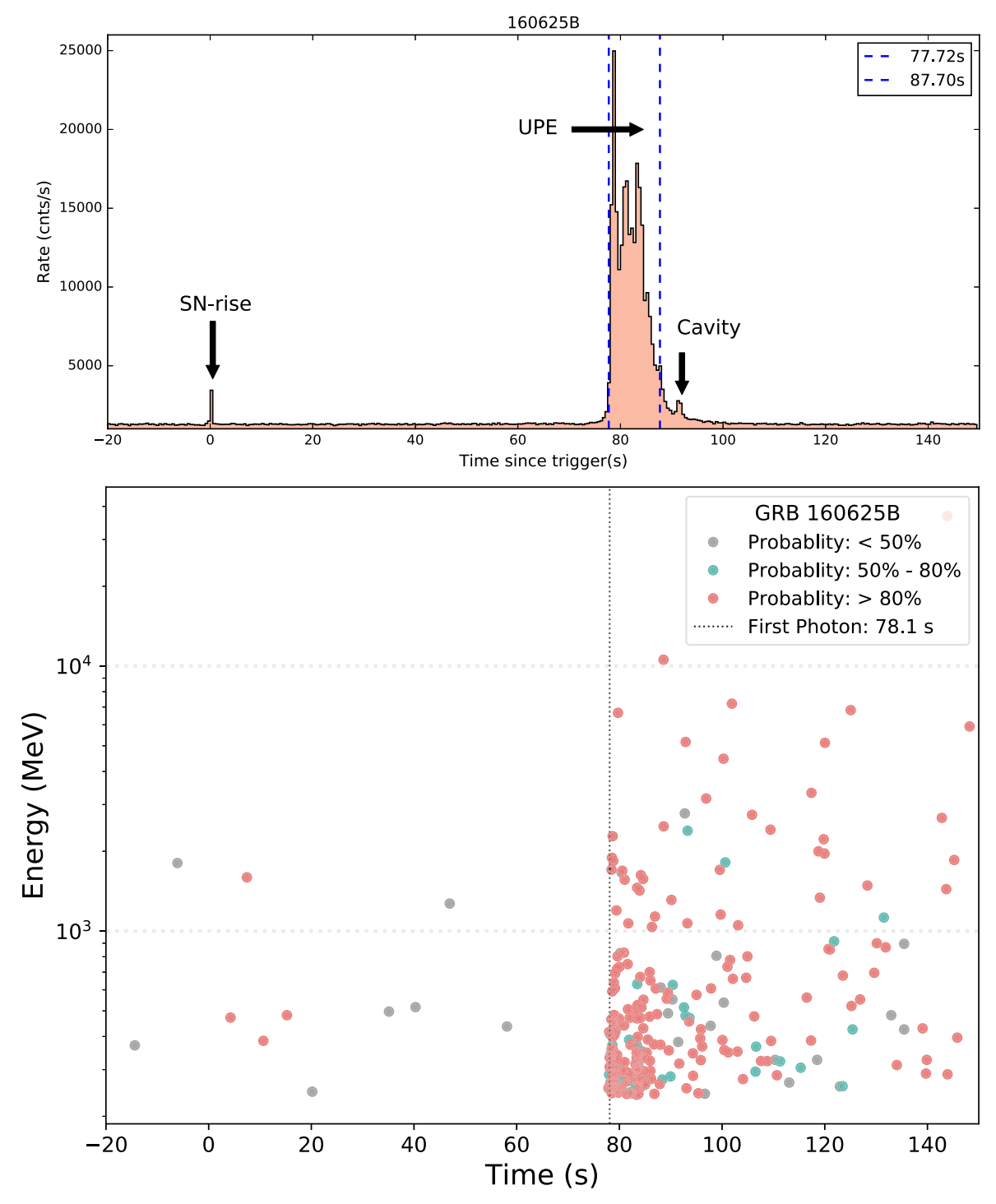


Figure 2. Upper panel: the proposed three new episodes of GRB 160625B as a function of the rest-frame time. Episode 1 occurs from $t_{\rm rf} = 0$ s to $t_{\rm rf} = 0.83$ s. The initial weak pulse represents the SN-rise. Episode 2 occurs from $t_{\rm rf} = 77.72$ s to $t_{\rm rf} = 87.70$ s, and includes the UPE emission. Episode 3 occurs from $t_{\rm rf} = 87.70$ s to $t_{\rm rf} = 92.27$ s. The redshift for GRB 160625B is 1.406 (Xu et al. 2016). The light curve consists of two clear spikes; the isotropic energy in the first one is $(1.09 \pm 0.20) \times 10^{52}$ erg. The total energy is ≈3 × 10⁵⁴ erg. Lower panel: the rest-frame time and the energy of Fermi-LAT photons in the energy band 0.1−100 GeV. The first photon of the GeV emission occurs at $t_{\rm rf} = 78.1$ s. The onset of the GeV radiation coincides with the onset of the UPE. Detailed information for each episode (SN-rise, UPE phase, cavity, GeV, and afterglow emission) is given in Section 3 and Table 1, which includes the typical starting time, the ending time, the isotropic energy, and the preferred model.

SN-rise of GRB 160509A is best fitted by a CPL + BB model, from $t_{\rm rf} \simeq 0.92 {\rm s}$ to $t_{\rm rf} \simeq 1.84 {\rm s}$. The spectrum contains a BB component of temperature 25.61 keV and a photon index α of -1.22, with $E_{\rm c} = 1769.76 {\rm keV}$.

2. *UPE phase*. We perform the corresponding time-resolved spectral analysis from which we can see that the self-

similarity first discovered in GRB 190114C is confirmed in the case of GRB 160509A. For the first iteration, we present the best fit of the spectrum of the entire duration of the UPE from $t_{\rm rf} = 4.84$ s to $t_{\rm rf} = 8.53$ s (see Figure 8, first layer). We then divide the rest-frame time interval in half and again perform the same spectral analysis for the

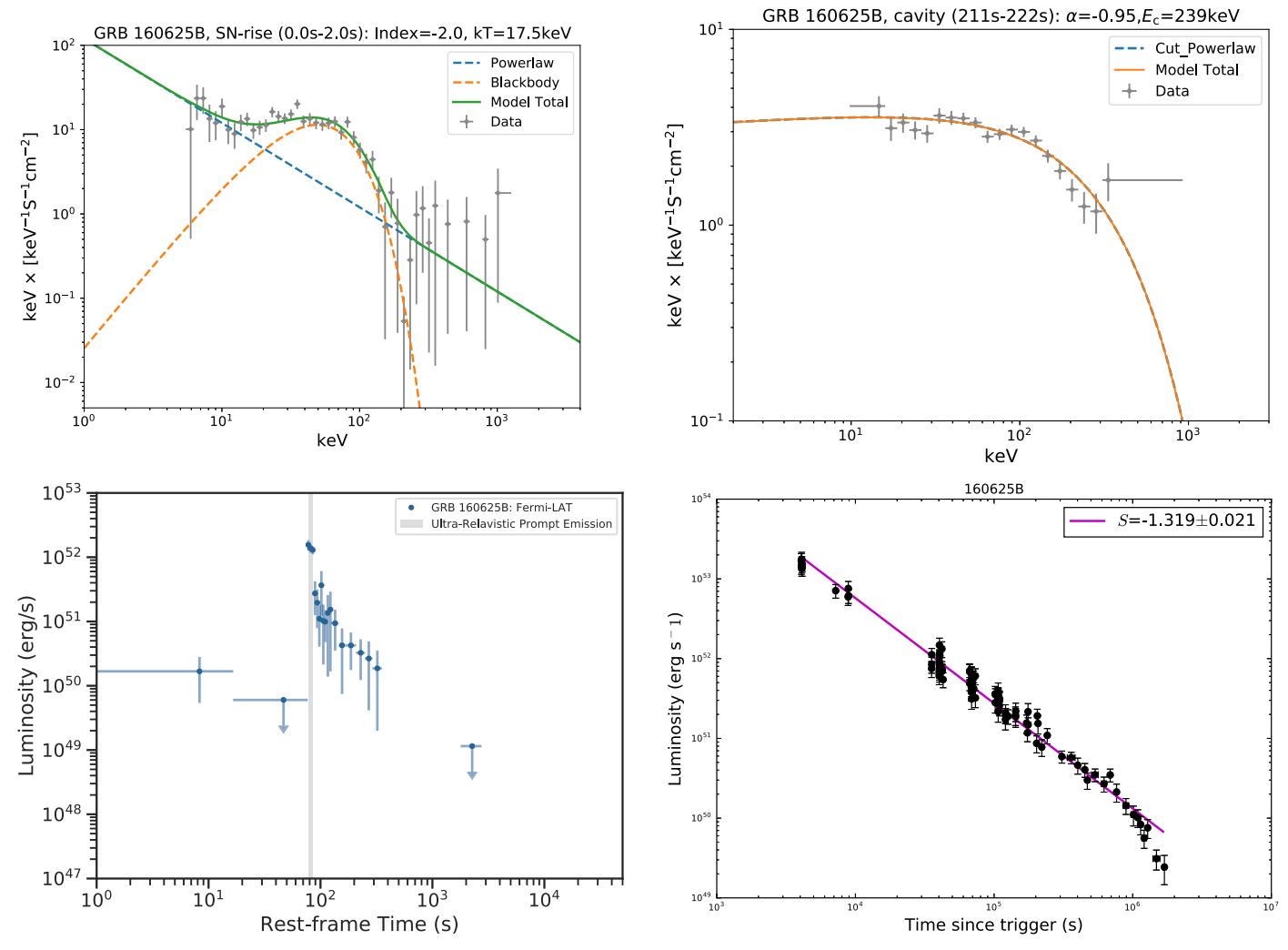


Figure 3. SN-rise, cavity, GeV, and afterglow of GRB 160625B; see also Table 1, which includes, for each episode, the starting time, the ending time, the isotropic energy, and the model that best fits the spectrum. Upper left: the spectrum of the SN-rise from 0 s to \approx 2.0 s ($t_{\rm rf}$ \approx 0.83 s). The spectrum is fitted by a blackbody of temperature 17.5 keV (in the observer's frame) plus a power law of index -2.0. Upper right: the cavity spectrum, from \approx 211 s ($t_{\rm rf}$ = 87.70 s) to \approx 222 s ($t_{\rm rf}$ = 92.27 s), is well fitted by a CPL, where the photon index α is -1.67 and the cutoff energy is 251 keV in the observer's frame. Lower left: Fermi-LAT rest-frame luminosity in the 100 MeV-100 GeV energy band (the UPE region is shaded gray). Lower right: k-corrected X-ray afterglow luminosity observed by Swift-XRT in the 0.3–10 keV band, as a function of the rest-frame time. It is best fitted by a power law with index 1.319 \pm 0.021.

Table 1
Episodes of GRB 160625B, Including the Starting Time, the Ending Time, the Energy (Isotropic), the Preferred Spectral Model, and the References

Episode	Starting Time Rest-frame	Ending Time Rest-frame	Energy	Spectrum	References
	(s)	(s)	(erg)		
SN-rise	0	0.83	1.09×10^{52}	CPL + BB	this paper
UPE	77.72	87.70	4.53×10^{54}	CPL + BB	this paper
Cavity	87.70	92.27	2.79×10^{52}	CPL	this paper
GeV	78.1	>300	2.99×10^{53}	PL	this paper
Afterglow	4082	>10 days	1.08×10^{53}	PL	this paper

Note. For the starting time of GeV emission, we take the time of the first GeV photon from the BH. The GeV emission may last for a very long time, but the observational time is limited because Fermi-LAT is not capable of resolving the late-time low-flux emission; therefore the ending time of GeV observation in the table is a lower limit. The starting time of X-ray afterglow in the table is taken from the starting time of Swift-XRT. The energy in the afterglow is integrated from 10^2 to 10^6 s. All times are given in the rest frame.

two 1.85 s intervals, i.e., [4.84–6.68 s] and [6.68–8.53 s], obtaining the results shown in Figure 8. Iteration 3: we then divide each of these half intervals in half again, i.e., $\Delta t_{\rm rf} = 0.92$ s corresponding to [4.84–5.76 s], [5.76–6.68 s],

[6.68–7.60 s], and [7.60–8.53 s], and redo the previous spectral analysis, obtaining the results still in Figure 8. In a fourth iteration we divide the UPE into eight subintervals of $\Delta t_{\rm rf} = 0.46$ s corresponding to the time intervals [4.84–5.30

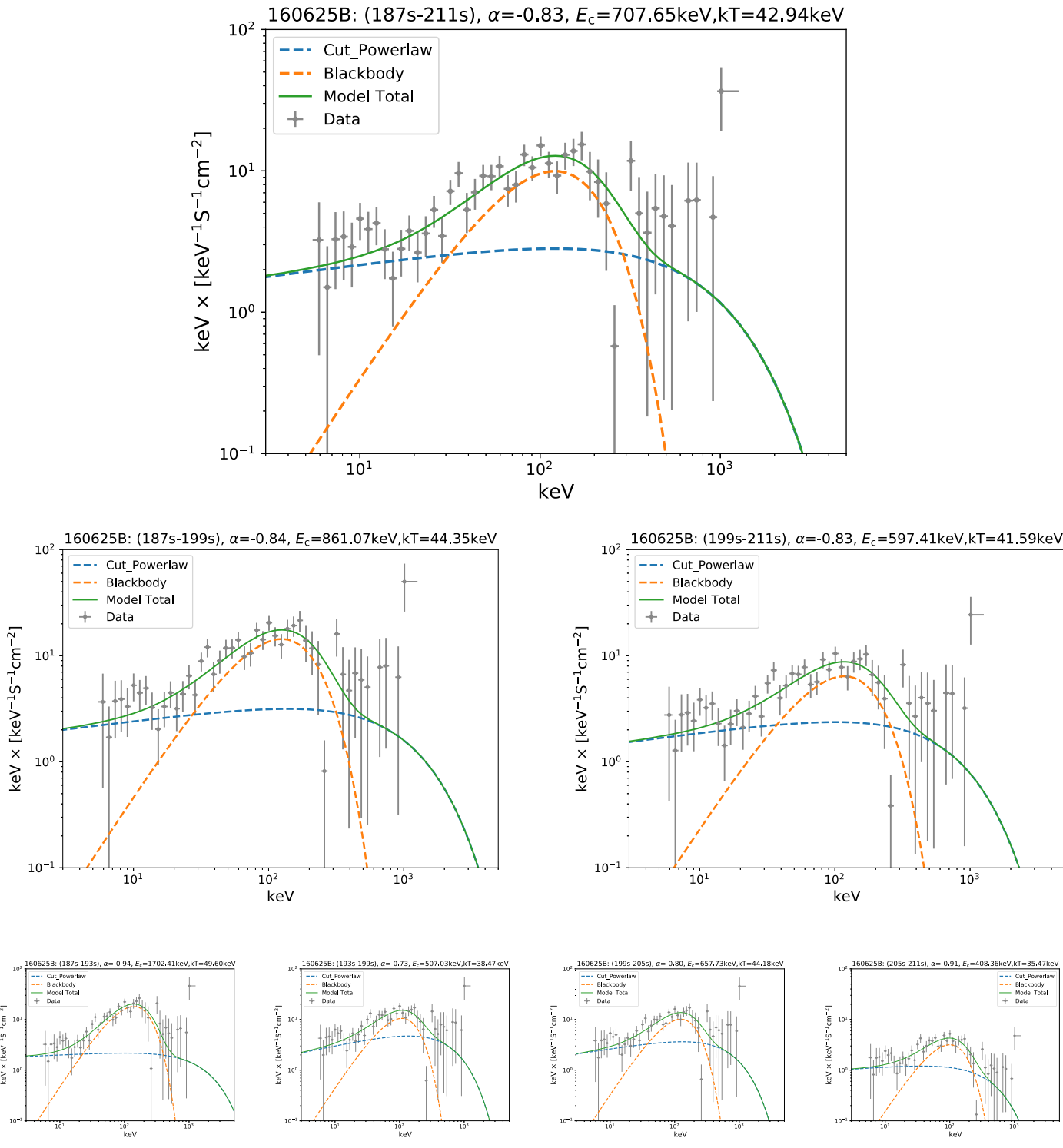


Figure 4. Time-resolved spectral analysis of GRB 160625B. All the layers have the same time coverage, from ≈ 187 s ($t_{rf} = 77.72$ s) to ≈ 211 s ($t_{rf} = 87.70$ s), but with different time divisions: one interval (top layer), two equal parts (second layer), four equal parts (third layer), eight equal parts (fourth and fifth layers), and sixteen equal parts (sixth, seventh, eighth, and ninth layers), respectively. The results of spectral analysis including duration, temperature, and cutoff energy are obtained in the observed frame, as shown in this figure. We have converted them to get their corresponding values in the rest frame: Table 2 shows the rest-frame time in column 2 and the rest-frame temperature in column 6.

s], [5.30–5.76 s], [5.76–6.22 s], [6.22–6.68 s], [6.68–7.14 s], [7.14–7.60 s], [7.60–8.06 s], and [8.06–8.53 s], and redo the spectral analysis (see Figure 8). In the fifth and final iteration of this process we divide the UPE into 16 subintervals of $\Delta t_{\rm rf} = 0.23$ s and we perform the corresponding spectral analysis and find the self-similar CPL +

BB emission in the time intervals [4.84–5.07 s], [5.07–5.30 s], [5.30–5.53 s], [5.53–5.76 s], [5.76–5.99 s], [5.99–6.22 s], [6.22–6.45 s], [6.45–6.68 s], [6.68–6.91 s], [6.91–7.14 s], [7.14–7.37 s], [7.37–7.60 s], [7.60–7.83 s], [7.83–8.06 s], [8.06–8.29 s], and [8.29–8.53 s]; see Figure 8. Figure 9 shows the luminosity of the Fermi-GBM as a function of

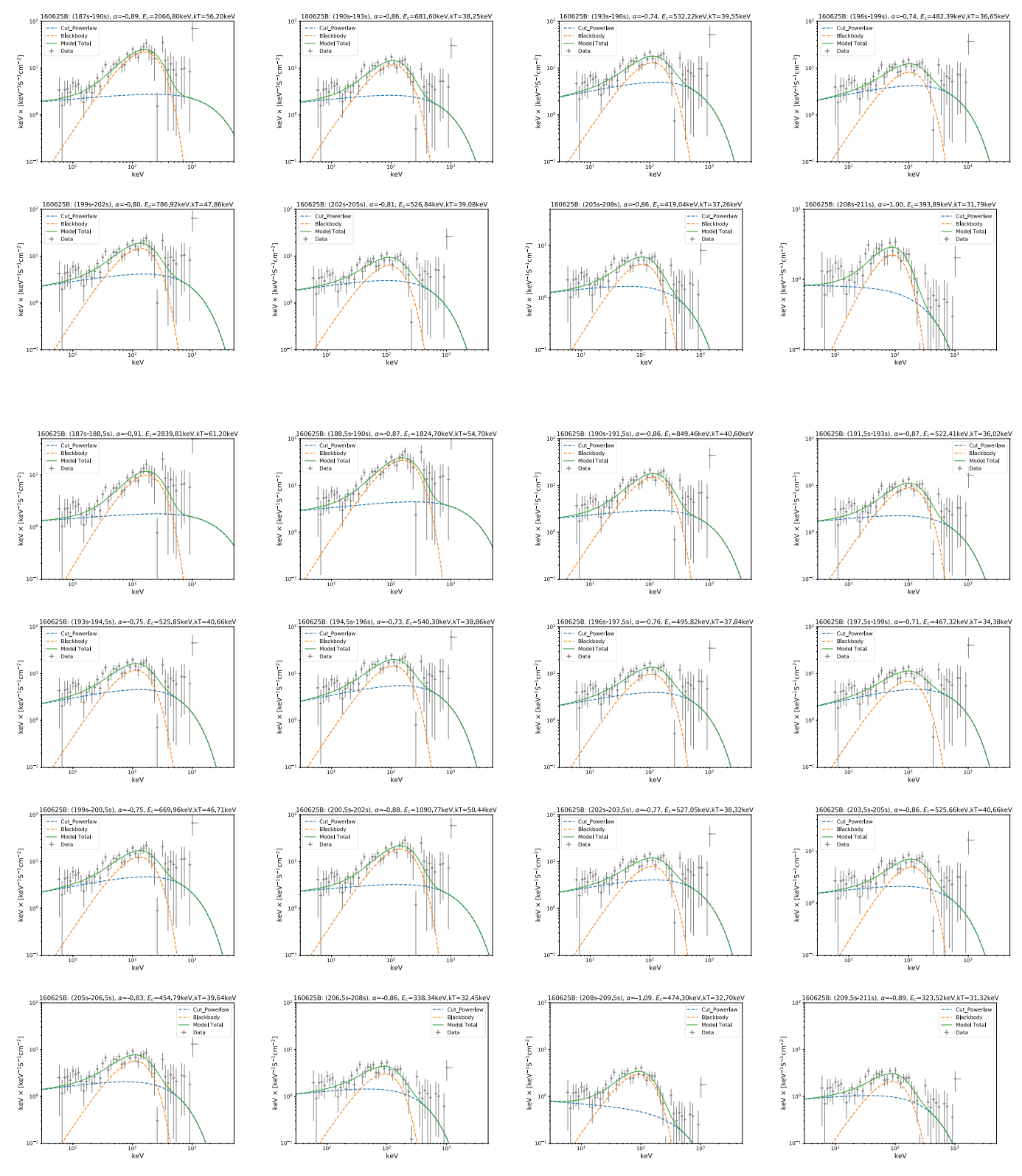


Figure 4. (Continued.)

the rest-frame time, derived from the fifth iteration (see Table 4). We also show the corresponding evolution of the rest-frame temperature (Figure 9). The best-fit parameters for each spectrum (α , $E_{\rm c}$), along with its time interval, Δ DIC, blackbody temperature kT, blackbody flux ($F_{\rm BB}$),

- total flux ($F_{\rm total}$), ratio of thermal to total flux, and the total energy are summarized in Table 4.
- 3. *Cavity*. Figure 7 (upper right panel) shows the spectral fitting of the cavity emission during the rest-frame time interval of its occurrence, i.e., from $t_{\rm rf} = 10.14$ to 13.82 s.

Table 2
Results of the Time-resolved Spectral Fits of GRB 160625B (CPL + BB Model) from $t_{rf} = 77.72$ s to $t_{rf} = 87.70$ s

$t_1 \sim t_2$	$t_{ m rf,1} \sim t_{ m rf,2}$	S	α	E _c	kT	ΔDIC	F _{BB}	F_{tot}	$F_{ m ratio}$	E_{tot}
(s) Obs.	(s) Rest-frame			(keV)	(keV) Rest-frame		(10^{-6}) (erg cm ⁻² s ⁻¹)	(10^{-6}) (erg cm ⁻² s ⁻¹)		(erg)
$187.00 \sim 211.00$	$77.72 \sim 87.70$	649.12	$-0.83^{+0.01}_{-0.01}$	$707.6^{+13.0}_{-12.9}$	$42.9_{-0.4}^{+0.4}$	-2840.2	$3.13^{+0.16}_{-0.15}$	$35.50^{+0.81}_{-0.87}$	$0.09^{+0.0}_{-0.0}$	4.53e+54
$187.00 \sim 199.00$	$77.72 \sim 82.71$	566.19	$-0.84^{+0.01}_{-0.01}$	861.1+20.8	44.4 ^{+0.5} _{-0.5}	-2789.1	$4.67^{+0.23}_{-0.24}$	$48.44^{+1.41}_{-1.40}$	$0.10^{+0.01}_{-0.01}$	3.09e+54
$199.00 \sim 211.00$	$82.71 \sim 87.70$	421.10	$-0.83^{+0.01}_{-0.01}$	$597.4_{-15.9}^{+15.8}$	$41.6_{-0.8}^{+0.8}$	-716.6	$1.95^{+0.18}_{-0.18}$	$24.53^{+0.83}_{-0.87}$	$0.08^{+0.01}_{-0.01}$	1.57e+54
$187.00 \sim 193.00$	$77.72 \sim 80.22$	426.56	$-0.94^{+0.01}_{-0.01}$	$1702.4^{+42.5}_{-42.7}$	$49.6_{-0.5}^{+0.5}$	-2935.0	$6.51^{+0.35}_{-0.32}$	$69.51^{+1.80}_{-1.92}$	$0.09^{+0.01}_{-0.01}$	2.22e+54
$193.00 \sim 199.00$	$80.22 \sim 82.71$	421.75	$-0.73^{+0.01}_{-0.01}$	$507.0^{+12.2}_{-12.4}$	$38.5^{+0.8}_{-0.8}$	-784.9	$2.95^{+0.30}_{-0.28}$	$37.46^{+1.33}_{-1.31}$	$0.08^{+0.01}_{-0.01}$	1.19e + 54
$199.00 \sim 205.00$	$82.71 \sim 85.20$	409.24	$-0.80^{+0.01}_{-0.01}$	$657.7^{+18.1}_{-18.6}$	$44.2^{+0.9}_{-0.9}$	-729.7	$3.25^{+0.35}_{-0.28}$	$40.93^{+1.57}_{-1.59}$	$0.08^{+0.01}_{-0.01}$	1.31e+54
$205.00 \sim 211.00$	$85.20 \sim 87.70$	205.28	$-0.91\substack{+0.02 \\ -0.02}$	$408.4^{+25.3}_{-25.8}$	$35.5^{+1.4}_{-1.4}$	-105.6	$0.82^{+0.17}_{-0.15}$	$9.08^{+0.75}_{-0.68}$	$0.09^{+0.02}_{-0.02}$	2.90e+53
$187.00 \sim 190.00$	$77.72 \sim 78.97$	344.58	$-0.89\substack{+0.01 \\ -0.01}$	$2066.8^{+50.1}_{-50.0}$	$56.2^{+0.7}_{-0.7}$	-2860.2	$9.08^{+0.63}_{-0.55}$	$105.00^{+3.03}_{-3.29}$	$0.09^{+0.01}_{-0.01}$	1.67e+54
$190.00 \sim 193.00$	$78.97 \sim 80.22$	282.28	$-0.86^{+0.01}_{-0.01}$	$681.6^{+31.2}_{-31.7}$	$38.2^{+0.8}_{-0.8}$	-603.9	$3.30^{+0.37}_{-0.35}$	$32.41^{+1.93}_{-1.63}$	$0.10^{+0.01}_{-0.01}$	5.17e+53
$193.00 \sim 196.00$	$80.22 \sim 81.46$	333.07	$-0.74^{+0.01}_{-0.01}$	$532.2^{+17.1}_{-17.0}$	$39.5^{+0.9}_{-1.0}$	-546.1	$3.76^{+0.51}_{-0.42}$	$43.09^{+2.07}_{-1.84}$	$0.09^{+0.01}_{-0.01}$	6.87e+53
$196.00 \sim 199.00$	$81.46 \sim 82.71$	287.45	$-0.74^{+0.01}_{-0.01}$	$482.4^{+16.9}_{-16.5}$	$36.6^{+1.3}_{-1.3}$	-287.5	$2.17^{+0.45}_{-0.34}$	$32.03^{+1.67}_{-1.50}$	$0.07^{+0.01}_{-0.01}$	5.11e+53
$199.00 \sim 202.00$	$82.71 \sim 83.96$	341.22	$-0.80\substack{+0.01 \\ -0.01}$	$786.9^{+29.1}_{-29.2}$	$47.9^{+1.0}_{-1.0}$	-661.0	$5.16^{+0.56}_{-0.50}$	$56.34^{+3.11}_{-2.55}$	$0.09^{+0.01}_{-0.01}$	8.99e + 53
$202.00 \sim 205.00$	$83.96 \sim 85.20$	258.65	$-0.81^{+0.02}_{-0.02}$	$526.8^{+21.7}_{-21.7}$	$39.1^{+1.5}_{-1.5}$	-181.9	$1.79^{+0.34}_{-0.31}$	$26.95^{+1.52}_{-1.45}$	$0.07^{+0.01}_{-0.01}$	4.30e + 53
$205.00 \sim 208.00$	$85.20 \sim 86.45$	182.22	$-0.86^{+0.03}_{-0.03}$	$419.0^{+28.9}_{-28.9}$	$37.3^{+1.7}_{-1.6}$	-90.1	$1.20^{+0.27}_{-0.27}$	$12.55^{+1.16}_{-1.06}$	$0.10^{+0.02}_{-0.02}$	2.00e + 53
$208.00 \sim 211.00$	$86.45 \sim 87.70$	116.10	$-1.00^{+0.04}_{-0.04}$	$393.9^{+46.2}_{-47.4}$	$31.8^{+2.1}_{-2.1}$	-37.9	$0.51^{+0.19}_{-0.15}$	$5.63^{+0.84}_{-0.67}$	$0.09^{+0.04}_{-0.03}$	8.97e+52
$187.00 \sim 188.50$	$77.72 \sim 78.35$	147.15	$-0.91\substack{+0.01 \\ -0.01}$	$2839.8^{+140.7}_{-141.4}$	$61.2^{+1.8}_{-1.8}$	-706.0	$4.47^{+0.74}_{-0.59}$	$63.65^{+3.89}_{-3.71}$	$0.07^{+0.01}_{-0.01}$	5.08e+53
$188.50 \sim 190.00$	$78.35 \sim 78.97$	354.91	$-0.87^{+0.01}_{-0.01}$	$1824.7^{+49.3}_{-49.4}$	$54.7^{+0.8}_{-0.8}$	-2291.1	$13.77^{+1.02}_{-0.93}$	$147.60^{+4.86}_{-5.17}$	$0.09^{+0.01}_{-0.01}$	1.18e + 54
$190.00 \sim 191.50$	$78.97 \sim 79.59$	227.35	$-0.86^{+0.02}_{-0.02}$	$849.5^{+52.9}_{-53.5}$	$40.6^{+1.1}_{-1.1}$	-465.8	$4.46^{+0.63}_{-0.58}$	$45.19^{+3.19}_{-3.25}$	$0.10^{+0.02}_{-0.01}$	3.60e + 53
$191.50 \sim 193.00$	$79.59 \sim 80.22$	181.28	$-0.87^{+0.03}_{-0.03}$	$522.4_{-37.6}^{+37.1}$	$36.0^{+1.4}_{-1.4}$	-178.9	$2.34^{+0.48}_{-0.42}$	$21.81^{+2.08}_{-1.89}$	$0.11^{+0.02}_{-0.02}$	1.74e + 53
$193.00 \sim 194.50$	$80.22 \sim 80.84$	229.41	$-0.75^{+0.02}_{-0.02}$	$525.9_{-25.2}^{+25.5}$	$40.7^{+1.5}_{-1.5}$	-223.5	$3.48^{+0.69}_{-0.62}$	$38.84^{+2.72}_{-2.41}$	$0.09^{+0.02}_{-0.02}$	3.10e + 53
$194.50 \sim 196.00$	$80.84 \sim 81.46$	254.52	$-0.73^{+0.02}_{-0.02}$	$540.3_{-23.0}^{+23.0}$	$38.9_{-1.2}^{+1.2}$	-338.7	$4.12^{+0.67}_{-0.58}$	$47.26^{+3.01}_{-2.65}$	$0.09^{+0.02}_{-0.01}$	3.77e + 53
$196.00 \sim 197.50$	$81.46 \sim 82.09$	212.08	$-0.76^{+0.02}_{-0.02}$	$495.8^{+24.6}_{-24.4}$	$37.8^{+1.6}_{-1.6}$	-188.9	$2.65^{+0.55}_{-0.49}$	$31.87^{+2.17}_{-2.17}$	$0.08^{+0.02}_{-0.02}$	2.54e + 53
$197.50 \sim 199.00$	$82.09 \sim 82.71$	205.41	$-0.71^{+0.02}_{-0.02}$	$467.3^{+22.3}_{-22.4}$	$34.4^{+2.2}_{-2.2}$	-114.0	$1.72^{+0.60}_{-0.51}$	$32.16^{+2.31}_{-2.18}$	$0.05^{+0.02}_{-0.02}$	2.56e + 53
$199.00 \sim 200.50$	$82.71 \sim 83.33$	239.62	$-0.75^{+0.02}_{-0.02}$	$670.0_{-31.3}^{+31.7}$	$46.7^{+1.6}_{-1.6}$	-256.6	$4.24^{+0.73}_{-0.65}$	$50.78^{+3.52}_{-3.33}$	$0.08^{+0.02}_{-0.01}$	4.05e + 53
$200.50 \sim 202.00$	$83.33 \sim 83.96$	256.45	$-0.88^{+0.02}_{-0.02}$	$1090.8^{+73.8}_{-74.6}$	$50.4^{+1.3}_{-1.2}$	-458.5	$6.88^{+0.91}_{-0.81}$	$66.21^{+5.27}_{-4.91}$	$0.10^{+0.02}_{-0.01}$	5.28e + 53
$202.00 \sim 203.50$	$83.96 \sim 84.58$	215.38	$-0.77\substack{+0.02 \\ -0.02}$	$527.0_{-25.2}^{+25.3}$	$38.3^{+1.8}_{-1.8}$	-132.1	$2.18^{+0.54}_{-0.44}$	$34.45^{+2.53}_{-2.25}$	$0.06^{+0.02}_{-0.01}$	2.75e + 53
$203.50 \sim 205.00$	$84.58 \sim 85.20$	157.84	$-0.86^{+0.03}_{-0.03}$	$525.7^{+39.3}_{-39.2}$	$40.1_{-2.4}^{+2.4}$	-63.6	$1.43^{+0.46}_{-0.37}$	$19.61^{+2.12}_{-1.73}$	$0.07^{+0.02}_{-0.02}$	1.56e + 53
$205.00 \sim 206.50$	$85.20 \sim 85.83$	150.18	$-0.83^{+0.03}_{-0.03}$	$454.8_{-37.9}^{+37.1}$	$39.6^{+2.0}_{-2.0}$	-71.7	$1.63^{+0.47}_{-0.39}$	$16.59^{+1.96}_{-1.59}$	$0.10^{+0.03}_{-0.03}$	1.32e + 53
$206.50 \sim 208.00$	$85.83 \sim 86.45$	112.49	$-0.86^{+0.05}_{-0.05}$	$338.3^{+41.3}_{-40.5}$	$32.5^{+2.9}_{-2.9}$	-29.1	$0.70^{+0.39}_{-0.27}$	$8.59^{+1.40}_{-1.15}$	$0.08^{+0.05}_{-0.03}$	6.85e + 52
$208.00 \sim 209.50$	$86.45\sim87.07$	84.98	$-1.09^{+0.06}_{-0.06}$	$474.3^{+88.9}_{-88.7}$	$32.7^{+2.2}_{-2.2}$	-34.0	$0.70^{+0.28}_{-0.21}$	$5.46^{+1.27}_{-0.84}$	$0.13^{+0.06}_{-0.04}$	4.35e + 52
$209.50 \sim 211.00$	$87.07 \sim 87.70$	82.67	$-0.89^{+0.06}_{-0.06}$	$323.5^{+52.4}_{-51.0}$	$31.3^{+3.4}_{-8.4}$	-58.7	$0.26^{+0.56}_{-0.19}$	$6.03^{+1.91}_{-1.15}$	$0.04^{+0.09}_{-0.03}$	4.81e+52

Note. This table reports: the time intervals in both rest frame and observer's frame, the significance (S) for each time interval, the power-law index, cutoff energy, temperature, Δ DIC, BB flux, total flux, ratio of BB to total flux $F_{\rm BB}/F_{\rm tot}$, and finally the isotropic energy. To select the best model from two different given models, we adopt the deviance information criterion, defined as DIC = $-2\log[p({\rm data}\,|\hat{\theta})] + 2p_{\rm DIC}$, where $\hat{\theta}$ is the posterior mean of the parameters and $p_{\rm DIC}$ is the effective number of parameters. The preferred model is the model with the lowest DIC score. Here we define Δ DIC = (CPL + BB) - CPL; if Δ DIC is negative it indicates that the CPL + BB is better. After comparing the DICs, we find the CPL + BB model is preferred to the CPL and other models. The Δ DIC scores are reported in column 7.

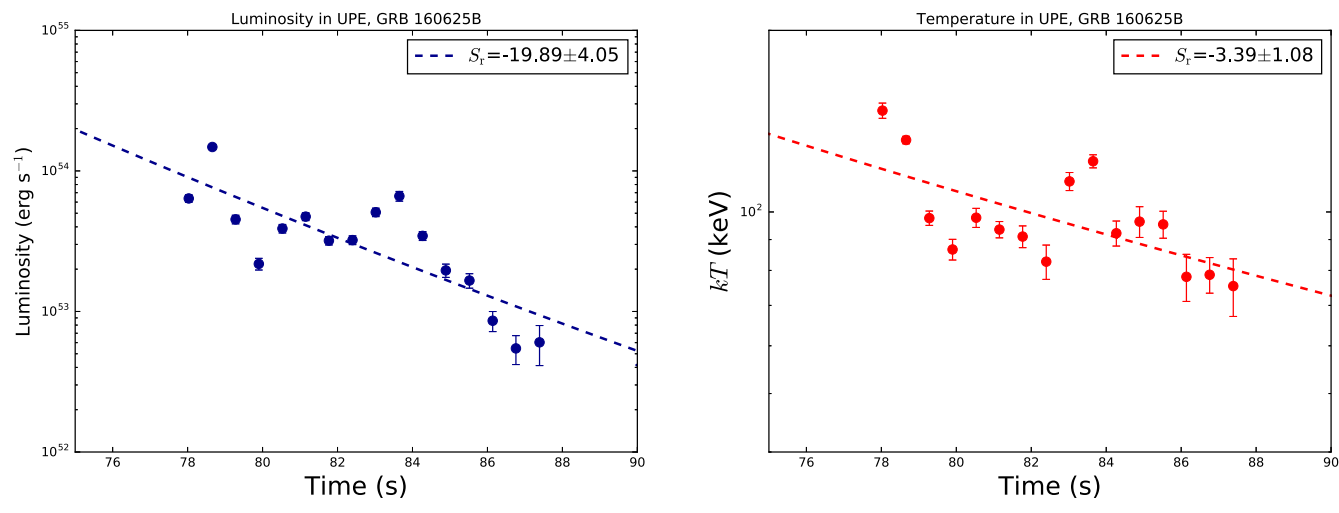


Figure 5. Left: light curve of the UPE of GRB 160625B derived from the fifth iteration with 16 subintervals. The values of the best-fit parameters from Table 2 are used to apply the k-correction and plot the rest-frame luminosity as a function of rest-frame time. The power-law index of the luminosity is -19.89 ± 4.05 . For more information about GeV luminosity behavior see Wang et al. (2019a). Right: corresponding rest-frame temperature of the UPE as a function of the rest-frame time.

The best fit of the spectrum is a CPL model with a photon index α of -1.20 and a cutoff energy of 314 keV.

- 4. *GeV emission*. Figure 7 (lower left panel) shows the luminosity of the GeV emission and the luminosity in the afterglow as a function of the rest-frame time.
- 5. Afterglow. Figure 7 (lower right panel) shows the (k-corrected) rest-frame afterglow luminosity (Swift/XRT data) as a function of rest-frame time. The best-fit parameters were obtained with a power-law index of -1.259 ± 0.025 .

5. GRB 130427A

A very bright burst, GRB 130427A, was announced by Fermi-GBM at 07:47:06.42 UT on 2013 April 27 (von Kienlin 2013). Swift-BAT was triggered 51.1 s later. Swift-UVOT and Swift-XRT began to observe at 181 and 195 s after the trigger (Maselli et al. 2013). Its redshift of z = 0.34 was detected and confirmed by the Gemini North telescope (Levan et al. 2013), Nordic Optical Telescope (Xu et al. 2013b), and VLT/X-shooter (Flores et al. 2013). The isotropic energy is 1.4×10^{54} erg, as detailed in Levan et al. (2013), von Kienlin (2013), Xu et al. (2013b), Flores et al. (2013), and Ruffini et al. (2015). A well observed fluence was recorded for GRB 130427A in the optical, X-ray, gamma-ray, and GeV bands. The Fermi-GBM count rate of GRB 130427A is shown in Figure 10. During the UPE phase the event count rate of n9 and n10 of Fermi-GBM surpasses $\sim 8 \times 10^4$ counts per second in the prompt radiation between rest-frame times $T_0 + 3.4$ s and $T_0 + 8.6 \,\mathrm{s}$. The GRB is there affected by pileup, 11 which significantly deforms the spectrum; details can be found in Ackermann et al. (2014) and Ruffini et al. (2015). Only the data between $t_{\rm rf} = 0.0$ and $t_{\rm rf} = 1.49 \, {\rm s}$ can be used for a spectral analysis in the prompt phase. As shown in Figure 10 (see also Table 5) clearly identified parts are:

1. *SN-rise*. Figure 11 (upper left panel) shows the clear identification of the SN-rise, as also reported in Figure 10. The spectrum of the SN-rise of GRB

130427A is best fitted by a CPL + BB model, from 0.0 s ($t_{\rm rf} \simeq 0.0 \, {\rm s}$) to 0.65 s ($t_{\rm rf} \simeq 0.49 \, {\rm s}$). The spectrum contains a BB component of temperature 42.63 keV and photon index $\alpha = -0.58$, and $E_{\rm c} = 547.59 \, {\rm keV}$.

- 2. *Cavity*. Figure 11 (upper right panel) shows the featureless spectrum of the cavity emission of GRB 130427A from $\approx 15 \, \text{s}$ ($t_{\rm rf} = 11.19 \, \text{s}$) to $\approx 25.5 \, \text{s}$ ($t_{\rm rf} = 19.03 \, \text{s}$); it is fitted by a CPL model with photon index $\alpha = -1.52$ and cutoff energy 496.13 keV.
- GeV emission. Figure 11 (lower left panel) shows the rest-frame luminosity of the GeV emission as a function of the rest-frame time.
- 4. Afterglow. Figure 11 (lower right panel) shows the (k-corrected) luminosity of the afterglow (Swift/XRT data) as a function of the rest-frame time, We apply the k-correction and measure the afterglow luminosity (Swift/XRT data) as a function of time; we obtain as best fit a power-law index of -1.276 ± 0.002 .

6. BdHN II: GRB 180728A

GRB 180728A triggered Swift-BAT at 17:29:00 UT on 2018 July 28 (Starling et al. 2018). Due to the Earth's limb, Swift-XRT began the observation 1730.8 s after the trigger (Perri et al. 2018). Fermi was triggered at 17:29:02.28 UT; no GeV photon was detected though the initial Fermi-LAT boresight angle was only 35° (Veres et al. 2018). This burst occurred at a close distance of redshift z = 0.117 and was detected by VLT/X-shooter (Rossi et al. 2018). On July 28, we made a prediction of the SN appearance in \sim 15 days (Ruffini et al. 2018a; Wang et al. 2019b), and indeed the SN optical peak was confirmed then (Izzo et al. 2018; Selsing et al. 2018). This GRB is composed of two pulses, see Figure 12 and Table 6.

1. First pulse as SN-rise. The first spike, the precursor, shows a power-law spectrum with a power-law index of -2.31 ± 0.08 in its 2.75 s duration. The averaged luminosity is $3.24^{+0.78}_{-0.55}\times10^{49}~\rm erg~s^{-1}$, and the integrated energy gives $7.98^{+1.92}_{-1.34}\times10^{49}~\rm erg$ in the range from 1 keV to 10 MeV. This energy emitted is in agreement

 $[\]overline{^{11}}$ Note that due to the pileup effect, the total energy of GRB 130427A has not been obtained.

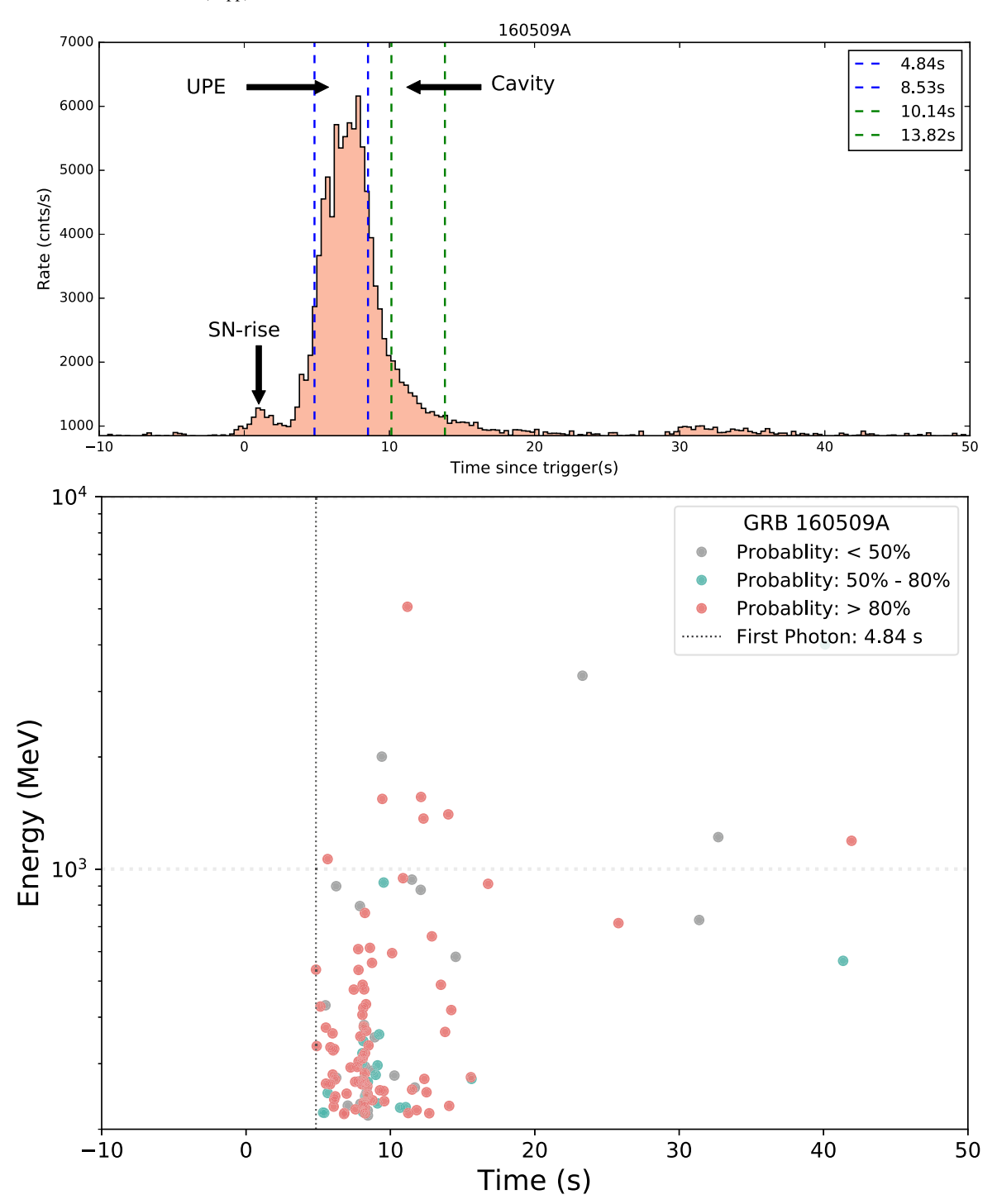


Figure 6. Upper panel: the proposed three new episodes of GRB 160509A as a function of the rest-frame time. Episode 1 occurs from $t_{\rm rf} = 0.92$ s to $t_{\rm rf} = 1.84$ s. Episode 2 including the UPE phase starts from $t_{\rm rf} = 4.84$ s and ends at $t_{\rm rf} = 8.53$ s in the rest frame. Episode 3 starts at $t_{\rm rf} = 10.14$ s and ends at $t_{\rm rf} = 13.82$ s. The redshift for GRB 160509A is 1.17 (Tanvir et al. 2016). The light curve consists of two spikes; the isotropic energy in the first small one is $\sim 1.47 \times 10^{52}$ erg. The total energy is 1.06×10^{54} erg (Tam et al. 2017). Lower panel: the energy and time of each Fermi-LAT photon of energy >100 MeV. The first GeV photon occurs at 4.84 s in the rest frame. The onset of the GeV radiation exactly coincides with the onset of the UPE. For detailed information on each episode (SN-rise, UPE phase, cavity, GeV, and Afterglow) see Section 4 and Table 3, which includes the starting time, the duration, the isotropic energy, and the preferred model.

with the conversion of the kinetic energy of SN-rise into electromagnetic emission.

2. Second pulse as the hypercritical accretion of the SN ejecta onto the companion NS. This pulse starts from 8.72 s, lasts 13.82 s, and contains 2.73×10^{51} erg isotropic energy. The best fit, which is a CPL + BB model of temperature \approx 7 keV in the observer's frame, is

shown in Figure 12. The BB component is interpreted as a matter outflow driven by the Rayleigh–Taylor convective instability developed in the accretion process (see, e.g., Izzo et al. 2012). From the time between observation of the SN-rise and the starting time of the hypercritical accretion, $\Delta t \approx 10 \, \mathrm{s}$, a binary separation of $\approx 3 \times 10^{10} \, \mathrm{cm}$ has been inferred. The binary separation determines, by

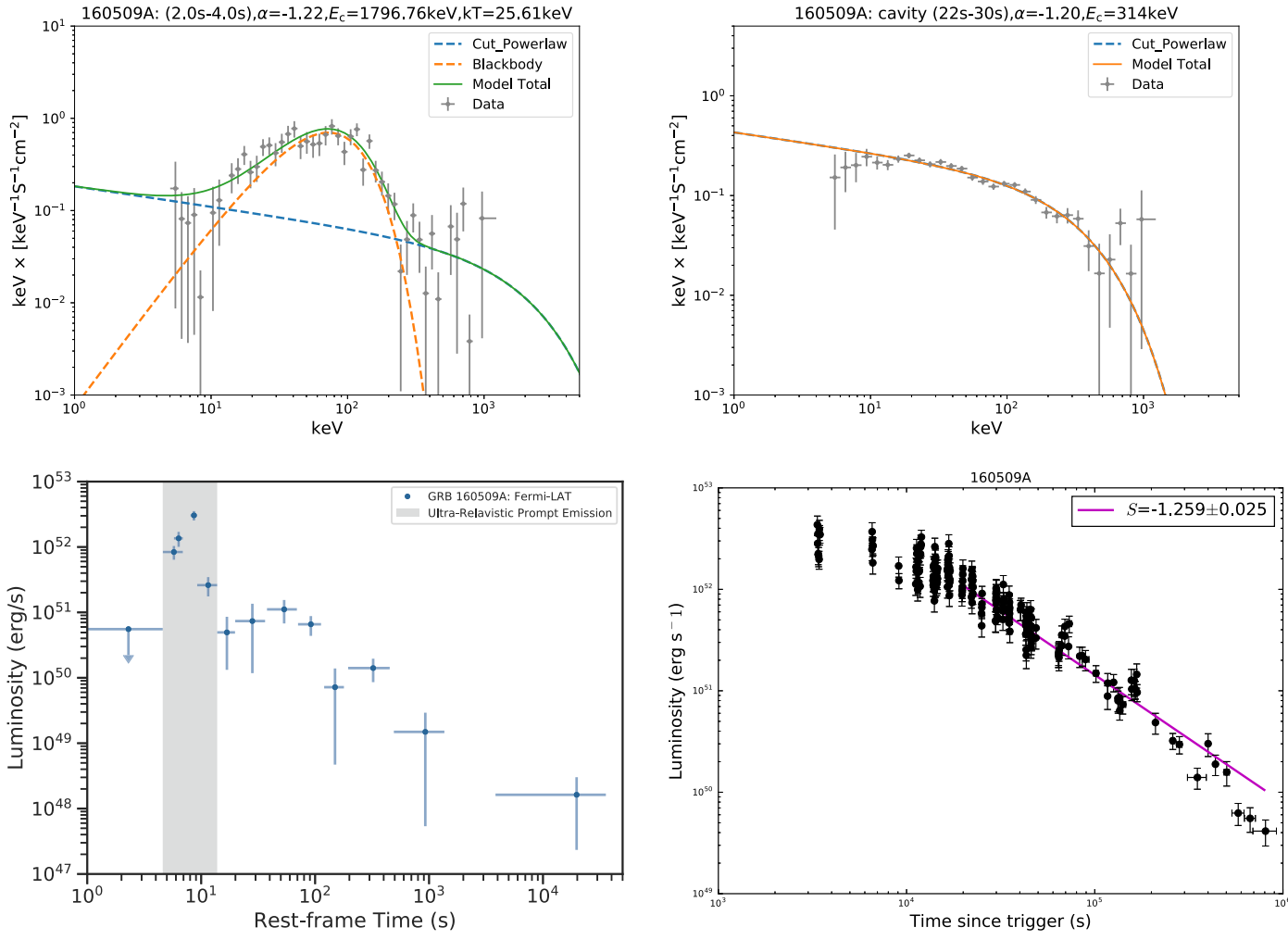


Figure 7. SN-rise, cavity, GeV, and afterglow of GRB 160509A; see also Table 3, which includes, for each episode, the starting time, the duration, the isotropic energy, and the model that best fits the spectrum. Upper left: The CPL + BB spectrum of the SN-rise, for the time interval from t=2.0 s ($t_{\rm rf}=0.92$ s) to t=4.0 s ($t_{\rm rf}=1.84$ s), spectral index $\alpha=-1.22$, cutoff energy $E_{\rm c}=1769.76$ keV, and temperature 25.61 keV in the observer's frame. Upper right: featureless spectrum of the cavity emission, fitted by a CPL model, from 22 s ($t_{\rm rf}=10.14$ s) to 30 s ($t_{\rm rf}=13.82$ s), where the photon index α is -1.20 and the cutoff energy is $E_{\rm c}=314$ keV in the observer's frame. Lower left: rest-frame Fermi-LAT light curve in the 100 MeV-100 GeV energy range. The UPE region is shaded gray. Lower right: k-corrected soft X-ray afterglow in the energy band 0.3–10 keV, observed by the Swift-XRT satellite, as a function of rest-frame time. It is best fitted by a power law with index 1.259 \pm 0.025.

 Table 3

 Episodes of GRB 160509A with the Parameters Defined as in Table 1

Episode	Starting Time Rest-frame	Ending Time Rest-frame	Energy (erg)	Spectrum	References
SN-rise	0.92 s	1.84 s	1.47×10^{52}	CPL + BB	New in this paper
UPE	4.84 s	8.53 s	1.06×10^{54}	CPL + BB	New in this paper
Cavity	10.14 s	13.82 s	3.66×10^{52}	CPL	New in this paper
GeV	4.84 s	$> 2 \times 10^4 \text{ s}$	3.59×10^{53}	PL	New in this paper
Afterglow	7287s	\sim 20 days	1.36×10^{52}	PL	New in this paper

angular momentum conservation, the spin period of ≈ 2.5 ms of the νNS left from the collapse of CO_{core} . This νNS powers the afterglow by dissipating its rotational energy (Wang et al. 2019b).

7. Discussion

In Table 7, we compare and contrast the duration, the fluxes, the energy, and the temperature of the BB component associated with the SN-rise of the above BdHNe I and II; we

also give, for each GRB, the corresponding redshift and $E_{\rm iso}$. In the case of BdHNe I, all of them have a similar SN-rise duration of nearly a second, consistent with the radius of the $\rm CO_{\rm core}$ of 10^{10} cm, and energies of the order of 10^{52} erg. These energies are much larger than the one we have found here in the SN-rise of BdHNe II, $\sim 10^{50}$ erg, which is comparable to that of isolated SNe (see, e.g., Arnett 1982; Bethe 1990; Waxman & Katz 2017). As listed in Table 7, the SN-rise energy $E_{\rm sh}$ for BdHNe I is of the order of 10^{52} erg, and for BdHNe II it is close to 10^{50} erg; both values are greater than the SN-rise energy of a

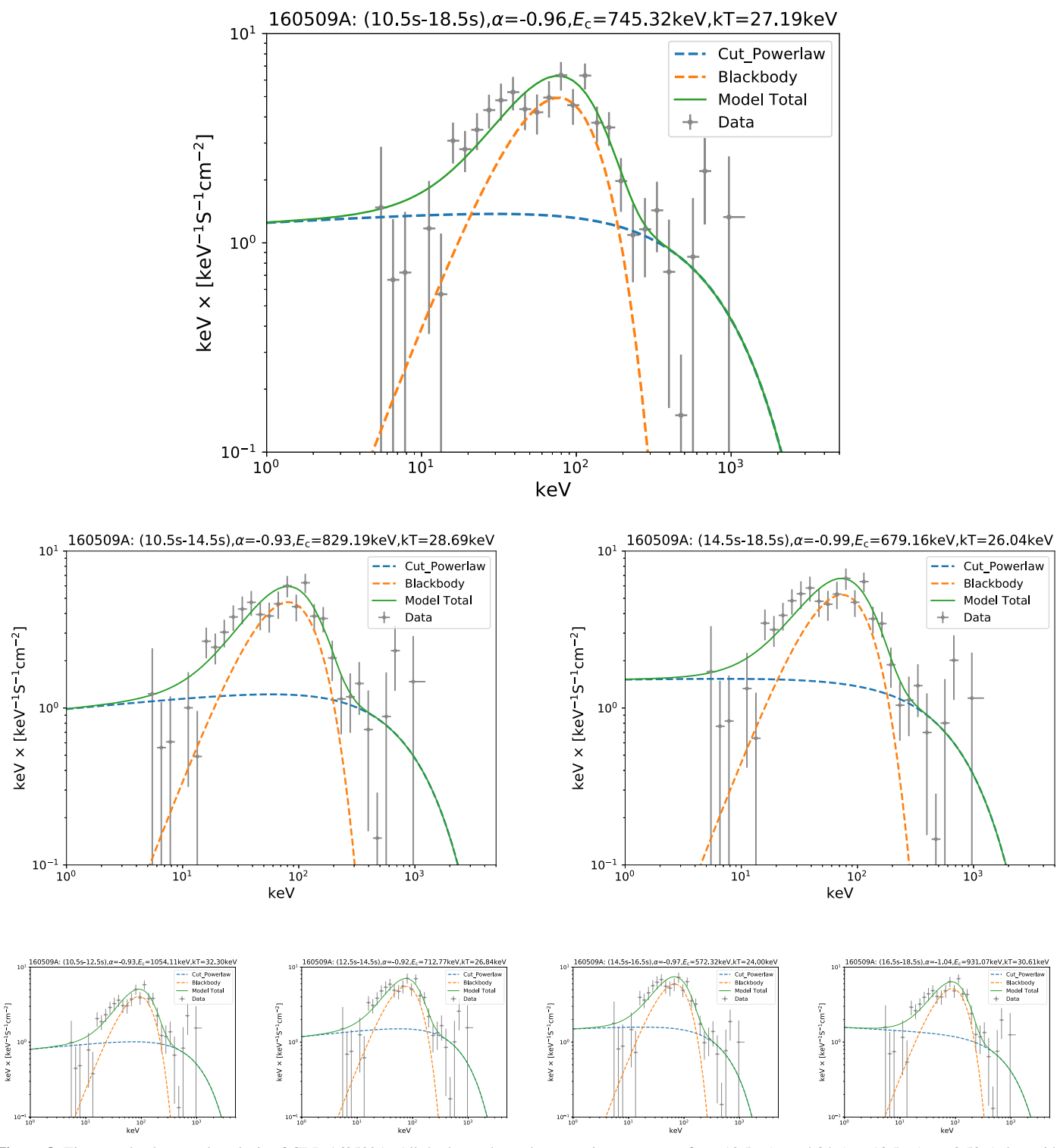


Figure 8. Time-resolved spectral analysis of GRB 160509A. All the layers have the same time coverage, from 10.5 s ($t_{\rm rf} = 4.84$ s) to 18.5 s ($t_{\rm rf} = 8.53$ s), but with different time divisions: one part (top layer), two equal parts (second layer), four equal parts (third layer), eight equal parts (fourth and fifth layers), and sixteen equal parts (sixth, seventh, eighth, and ninth layers), respectively. Two dashed lines represent CPL (blue) and BB (orange) components, while the solid line represents the total model (green). The results of spectral analysis including duration, temperature, and cutoff energy are obtained in the observed frame, as shown in this figure. We have converted them to get their corresponding values in the rest frame; Table 4 shows the rest-frame time in column 2, rest-frame cutoff energy in column 5, and rest-frame temperature in column 6.

normal SN (Bethe 1990; Waxman & Katz 2017). As we shall see below, such a difference can in principle be explained by a difference stemming from the configuration of the progenitors, such that the BdHN originated from a binary system, while a normal supernova originates from an isolated single star.

7.1. The SN-rise Energetics of BdHNe I

The larger energies of the SN-rise associated with BdHNe I discovered here can also be ascribed to a more energetic, rapidly rotating CO_{core}. This can be the result of the binary

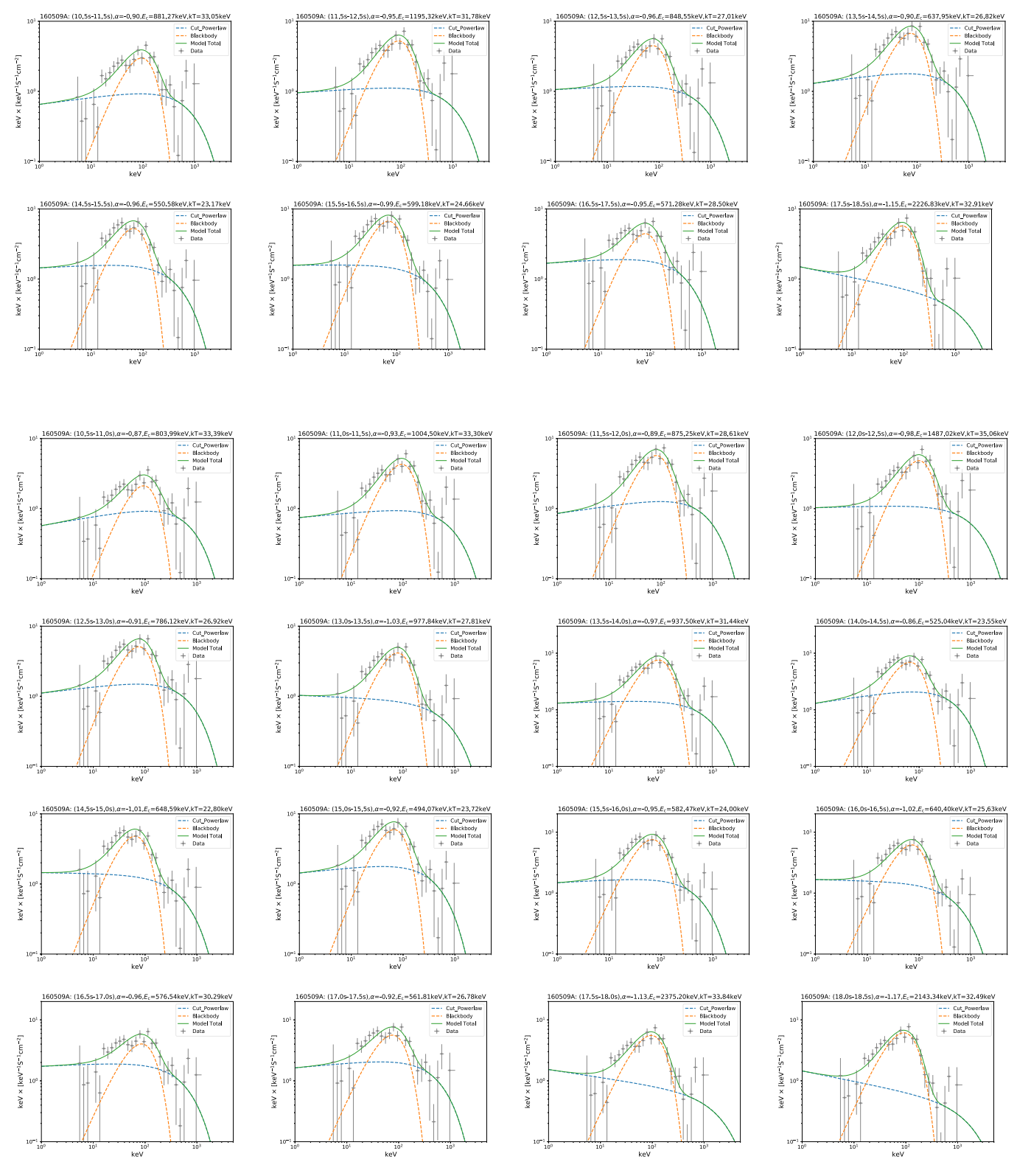


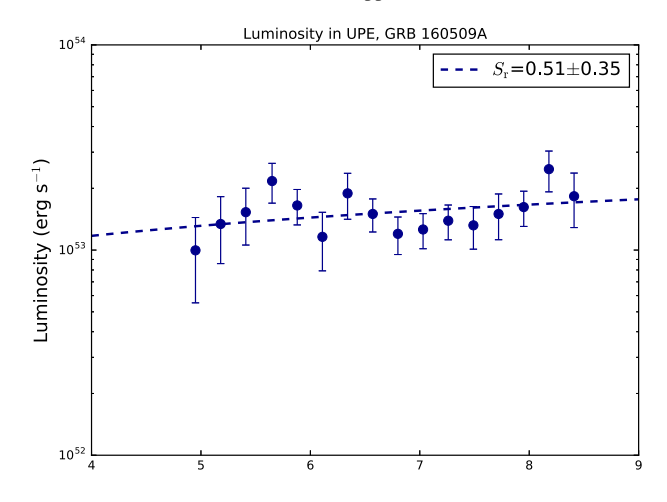
Figure 8. (Continued.)

nature of the progenitor with a short orbital period of the order of 4–5 minutes, in which angular momentum transfer by tidal effects during the previous evolutionary stages has been at work very efficiently.

Let us estimate the rotational energy of the CO_{core} assuming that the binary is tidally locked. In this case the rotation period

of the CO_{core} , P_{CO} , equals the binary orbital period, P_{orb} (see, e.g., Hurley et al. 2002), i.e.,

$$P_{\rm CO} = P_{\rm orb} = 2\pi \sqrt{\frac{a_{\rm orb}^3}{GM_{\rm tot}}},$$
(12)



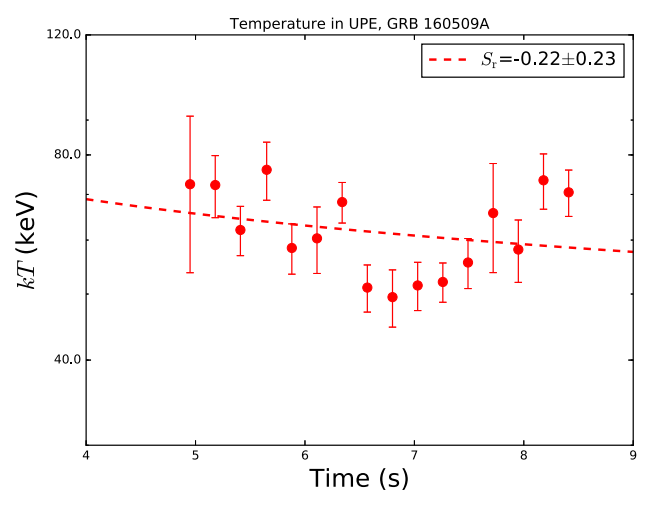


Figure 9. Left: luminosity light curve of the UPE of GRB 160509A as derived from the fifth iteration with 16 subintervals. The values of the best fit parameters from Table 4 are used to apply the k-correction and measure the luminosity as a function of time. The power-law index of 0.51 ± 0.35 for the luminosity is similar to the one obtained in the GeV emission luminosity after the UPE phase with index of -0.22 ± 0.23 . For more information about GeV luminosity behavior see Wang et al. (2019a). Right: evolution of the rest-frame temperature of the UPE as derived from the fifth iteration with 16 subintervals, as reported in Table 4.

which is related to the binary separation $a_{\rm orb}$ and the total mass of the system $M_{\rm tot}$; G is the gravitational constant. Let us adopt a typical progenitor of a BdHN from Becerra et al. (2019): a $\rm CO_{\rm core}$ obtained from the evolution of a $30\,M_\odot$ zero-age mainsequence (ZAMS) progenitor star, which has a total mass of $M_{\rm CO}=8.9\,M_\odot$ and radius $R_{\rm CO}=7.83\times10^9\,{\rm cm}$, and forms a binary with an NS companion of $M_{\rm NS}=2\,M_\odot$. As for the orbital period/separation, we constrain our systems by the condition that there is no Roche-lobe overflow at the moment of the supernova explosion of the $\rm CO_{\rm core}$. The Roche-lobe radius of the $\rm CO_{\rm core}$ can be estimated as (Eggleton 1983)

$$\frac{R_{\rm RL}}{a_{\rm orb}} = \frac{0.49q^{2/3}}{0.6q^{2/3} + \ln(1 + q^{1/3})},\tag{13}$$

where $q = M_{\rm CO}/M_{\rm NS}$. Therefore, the minimum orbital period of the binary, $a_{\rm orb,min}$, is obtained when $R_{\rm CO} = R_{\rm RL}$. For the above parameters, $a_{\rm orb,min} \approx 1.53 \times 10^{10}$ cm and correspondingly the minimum orbital period is $P_{\rm orb,min} \approx 5.23$ minutes.

The rotational energy for a CO_{core} is

$$E_{\text{rot,CO}} = \frac{1}{2} I_{\text{CO}} \omega_{\text{CO}}^2 = \frac{1}{2} I_{\text{CO}} \left(\frac{2\pi}{P_{\text{CO}}} \right)^2,$$
 (14)

where $I_{\rm CO}$ is the moment of inertia of the ${\rm CO}_{\rm core}$. So, adopting $P_{\rm CO}=P_{\rm orb,min}$ ($\omega_{\rm CO}\approx 0.03~{\rm rad\,s^{-1}}$) and $I_{\rm CO}\approx (2/5)M_{\rm CO}R_{\rm CO}^2$, we obtain $E_{\rm rot,CO}\approx 8.7\times 10^{49}$ erg. This is of course lower than the gravitational binding energy $|W|\approx (3/5)GM_{\rm CO}^2/R_{\rm CO}\approx 1.6\times 10^{51}$ erg and lower than the internal thermal energy as from the virial theorem. If we adopt the ${\rm CO}_{\rm core}$ from the $25\,M_{\odot}$ ZAMS progenitor (see Table 1 in Becerra et al. 2019), characterized by $M_{\rm CO}=6.85\,M_{\odot}$ and $R_{\rm CO}=5.86\times 10^9\,{\rm cm}$, and for the corresponding minimum orbital period $P_{\rm orb,min}\approx 4$ minutes ($\omega_{\rm CO}\approx 0.02~{\rm rad\,s^{-1}}$), we obtain $E_{\rm rot,CO}\approx 6.3\times 10^{49}\,{\rm erg}$.

Therefore, a much more energetic SN-rise can be the result of an exploding CO_{core} that rotates much faster than the rate set by tidal synchronization. In the above two examples, the ratio of rotational to gravitational energy is $E_{rot}/|W| \approx 0.05$.

However, from the stability point of view, it is known from the theory of Newtonian ellipsoids that secular axisymmetric instability sets in at $E_{\rm rot}/|W| \approx 0.14$ and dynamical instability at $E_{\rm rot}/|W| \approx 0.25$ (Chandrasekhar 1969).

Indeed, three-dimensional simulations of SN explosions confirm these stability limits and so explore SN explosions from pre-SN cores with high rotation rates of the order of 1 rad s⁻¹ (see, e.g., Nakamura et al. 2014; Gilkis 2018; Fujisawa et al. 2019). These angular velocities are a factor 30–50 faster than the ones we have considered above. This implies that the rotational energy of the pre-SN core can be up to a factor 10^3 higher, namely $E_{\rm rot} \sim {\rm few} \times 10^{52}$ erg.

7.2. The SN-rise Energetics of BdHNe II

In the case of BdHNe II, the SN-rise has been shown to have a much smaller energy, 10^{49} – 10^{50} erg. A similar case in the literature is represented by SN 2006aj, associated with GRB 060218 (Campana et al. 2006; Ferrero et al. 2006; Mirabal et al. 2006; Pian et al. 2006; Sollerman et al. 2006). The GRB 060218/SN 2006aj association was indeed interpreted in Becerra et al. (2016) as a BdHN II (at that time called "Xray flash"). As we have mentioned, the energetics of these SNrises are closer to the typical ones encountered in isolated SNe (see, e.g., Arnett 1982; Bethe 1990; Waxman & Katz 2017). This is consistent with the longer orbital periods of BdHNe II (Becerra et al. 2016) since, being farther apart, in the prior evolutionary stages binary interactions have been less effective in transferring angular momentum to the CO_{core}. This explains why the SNe associated with BdHNe II, even if they occur in a binary, are more similar to isolated SNe.

As a final remark, we recall that the occurrence of the SN is deduced from direct optical observations for GRB sources at z < 1, and for all cases the SN occurrence is also inferred, indirectly, from the observation of the afterglows. Indeed, the afterglow originates from the feedback of the emission of the ν NS, created in the SN event, into the expanding SN ejecta, given the proof of the SN occurrence (see Ruffini et al. 2018c; Rueda et al. 2020; Wang et al. 2019b, for details).

Table 4
Results of the Time-resolved Spectral Fits of GRB 160509A (CPL + BB Model) from $t_{\rm rf} = 4.84$ s to $t_{\rm rf} = 8.53$ s

$t_1 \sim t_2$ (s) Obs.	$t_{\rm rf,1} \sim t_{\rm rf,2}$ (s) Rest-frame	S	α	E _c (keV)	kT (keV)	ΔDIC	$F_{\rm BB}$ (10 ⁻⁶ erg cm ⁻² s ⁻¹)	F_{tot} (10 ⁻⁶ erg cm ⁻² s ⁻¹)	$F_{ m ratio}$	E _{tot} (erg)
$10.50 \sim 18.50$	4.84 ~ 8.53	292.18	$-0.96^{+0.01}_{-0.01}$	$745.3^{+27.6}_{-26.9}$	$27.2_{-0.6}^{+0.6}$	-633.8	$0.98^{+0.13}_{-0.11}$	$18.01^{+1.10}_{-1.00}$	$0.05^{+0.01}_{-0.01}$	5.40e+53
$10.50 \sim 14.50$	$4.84 \sim 6.68$	199.13	$-0.93^{+0.02}_{-0.02}$	829.2 ^{+47.6} _{-47.0}	$28.7^{+0.9}_{-0.9}$	-335.4	$1.00^{+0.19}_{-0.15}$	$18.50^{+1.70}_{-1.57}$	$0.05^{+0.01}_{-0.01}$	2.77e+53
$14.50 \sim 18.50$	$6.68 \sim 8.53$	232.97	$-0.99^{+0.01}_{-0.01}$	$679.2^{+31.9}_{-32.3}$	$26.0^{+0.8}_{-0.8}$	-324.2	$0.99^{+0.19}_{-0.15}$	$18.00^{+1.28}_{-1.27}$	$0.05^{+0.01}_{-0.01}$	2.70e+53
$10.50 \sim 12.50$	$4.84\sim5.76$	127.55	$-0.93^{+0.02}_{-0.02}$	$1054.1^{+97.5}_{-97.1}$	$32.3_{-1.7}^{+1.7}$	-145.5	$0.94^{+0.30}_{-0.22}$	$18.83^{+2.62}_{-2.40}$	$0.05^{+0.02}_{-0.01}$	1.41e+53
$12.50 \sim 14.50$	$5.76 \sim 6.68$	161.51	$-0.92^{+0.02}_{-0.02}$	$712.8^{+47.1}_{-47.4}$	$26.8^{+1.1}_{-1.1}$	-205.1	$1.08^{+0.26}_{-0.20}$	$18.81^{+1.96}_{-1.82}$	$0.06^{+0.01}_{-0.01}$	1.41e+53
$14.50 \sim 16.50$	$6.68 \sim 7.60$	169.80	$-0.97^{+0.02}_{-0.02}$	$572.3_{-33.2}^{+32.9}$	$24.0^{+1.0}_{-1.0}$	-203.4	$1.02^{+0.27}_{-0.20}$	$16.14^{+1.53}_{-1.39}$	$0.06^{+0.02}_{-0.01}$	1.21e+53
$16.50 \sim 18.50$	$7.60 \sim 8.53$	169.78	$-1.04^{+0.02}_{-0.02}$	$931.1^{+87.8}_{-86.6}$	$30.6^{+1.6}_{-1.6}$	-147.6	$1.15^{+0.31}_{-0.27}$	$20.87^{+2.83}_{-2.24}$	$0.06^{+0.02}_{-0.01}$	1.56e+53
$10.50 \sim 11.50$	$4.84\sim5.30$	77.67	$-0.90^{+0.04}_{-0.04}$	$881.3^{+135.4}_{-141.4}$	$33.0^{+3.3}_{-3.3}$	-43.8	$0.69^{+0.45}_{-0.27}$	$14.27^{+3.75}_{-2.93}$	$0.05^{+0.03}_{-0.02}$	5.35e+52
$11.50 \sim 12.50$	$5.30\sim5.76$	104.90	$-0.95^{+0.02}_{-0.02}$	$1195.3^{+126.1}_{-124.3}$	$31.8^{+1.9}_{-1.9}$	-117.1	$1.21^{+0.45}_{-0.33}$	$23.14^{+3.53}_{-3.11}$	$0.05^{+0.02}_{-0.02}$	8.67e + 52
$12.50 \sim 13.50$	$5.76\sim6.22$	102.77	$-0.96^{+0.03}_{-0.03}$	$848.5^{+91.0}_{-89.5}$	$27.0^{+1.8}_{-1.8}$	-81.4	$0.86^{+0.37}_{-0.25}$	$17.63^{+2.89}_{-2.59}$	$0.05^{+0.02}_{-0.02}$	6.61e+52
$13.50 \sim 14.50$	$6.22\sim6.68$	129.10	$-0.90\substack{+0.03 \\ -0.03}$	$638.0^{+53.1}_{-52.7}$	$26.8^{+1.4}_{-1.4}$	-128.1	$1.30^{+0.38}_{-0.31}$	$20.50^{+3.12}_{-2.65}$	$0.06^{+0.02}_{-0.02}$	7.68e + 52
$14.50 \sim 15.50$	$6.68 \sim 7.14$	117.25	$-0.96^{+0.03}_{-0.03}$	$550.6^{+44.3}_{-44.5}$	$23.2^{+1.5}_{-1.5}$	-85.7	$0.86^{+0.32}_{-0.26}$	$15.20^{+2.37}_{-1.68}$	$0.06^{+0.02}_{-0.02}$	5.69e + 52
$15.50 \sim 16.50$	$7.14 \sim 7.60$	127.21	$-0.99^{+0.03}_{-0.03}$	$599.2^{+52.7}_{-52.5}$	$24.7^{+1.3}_{-1.3}$	-124.5	$1.17^{+0.40}_{-0.28}$	$17.14^{+2.23}_{-2.19}$	$0.07^{+0.03}_{-0.02}$	6.42e + 52
$16.50 \sim 17.50$	$7.60 \sim 8.06$	131.95	$-0.95^{+0.03}_{-0.03}$	$571.3^{+47.4}_{-46.6}$	$28.5^{+2.3}_{-2.4}$	-49.8	$0.90^{+0.46}_{-0.34}$	$19.51^{+2.69}_{-2.19}$	$0.05^{+0.02}_{-0.02}$	7.31e + 52
$17.50 \sim 18.50$	$8.06\sim8.53$	112.19	$-1.15\substack{+0.02 \\ -0.02}$	$2226.8^{+325.2}_{-326.2}$	$32.9_{-1.9}^{+1.9}$	-133.0	$1.33^{+0.47}_{-0.34}$	$27.25^{+4.66}_{-3.82}$	$0.05^{+0.02}_{-0.01}$	1.02e + 53
$10.50 \sim 11.00$	$4.84\sim5.07$	48.87	$-0.87^{+0.06}_{-0.06}$	$804.0^{+189.6}_{-191.8}$	$33.4^{+8.6}_{-8.3}$	-23.1	$0.33^{+0.86}_{-0.24}$	$12.55^{+5.59}_{-3.97}$	$0.03^{+0.07}_{-0.02}$	2.35e+52
$11.00 \sim 11.50$	$5.07\sim5.30$	61.64	$-0.93^{+0.05}_{-0.05}$	$1004.5^{+202.6}_{-211.2}$	$33.3_{-3.5}^{+3.5}$	-40.8	$1.00^{+0.67}_{-0.42}$	$16.82^{+6.06}_{-4.34}$	$0.06^{+0.05}_{-0.03}$	3.15e + 52
$11.50 \sim 12.00$	$5.30\sim5.53$	74.34	$-0.89^{+0.05}_{-0.05}$	$875.2^{+145.3}_{-147.8}$	$28.6^{+2.4}_{-2.4}$	-64.6	$1.13^{+0.55}_{-0.37}$	$19.22^{+5.94}_{-4.13}$	$0.06^{+0.03}_{-0.02}$	3.60e + 52
$12.00 \sim 12.50$	$5.53\sim5.76$	75.45	$-0.98^{+0.03}_{-0.03}$	$1487.0^{+208.8}_{-205.9}$	$35.1^{+3.4}_{-3.4}$	-57.0	$1.16^{+0.74}_{-0.44}$	$27.26^{+6.00}_{-4.46}$	$0.04^{+0.03}_{-0.02}$	5.11e + 52
$12.50 \sim 13.00$	$5.76\sim5.99$	81.26	$-0.91^{+0.03}_{-0.03}$	$786.1^{+96.3}_{-96.7}$	$26.9^{+2.3}_{-2.3}$	-49.0	$0.94^{+0.54}_{-0.34}$	$20.82^{+4.08}_{-3.74}$	$0.05^{+0.03}_{-0.02}$	3.90e + 52
$13.00 \sim 13.50$	$5.99\sim6.22$	65.10	$-1.03^{+0.05}_{-0.05}$	$977.8^{+201.9}_{-199.4}$	$27.8^{+3.1}_{-3.1}$	-39.8	$0.77^{+0.62}_{-0.34}$	$14.55^{+4.63}_{-3.02}$	$0.05^{+0.05}_{-0.03}$	2.73e + 52
$13.50 \sim 14.00$	$6.22\sim6.45$	90.78	$-0.97^{+0.04}_{-0.04}$	$937.5^{+151.2}_{-151.4}$	$31.4^{+2.1}_{-2.1}$	-77.7	$1.62^{+0.68}_{-0.42}$	$23.85^{+6.01}_{-4.95}$	$0.07^{+0.03}_{-0.02}$	4.47e + 52
$14.00 \sim 14.50$	$6.45\sim6.68$	93.73	$-0.86^{+0.04}_{-0.04}$	$525.0^{+50.2}_{-49.4}$	$23.6^{+1.9}_{-1.9}$	-65.2	$1.13^{+0.61}_{-0.37}$	$18.94^{+3.46}_{-3.06}$	$0.06^{+0.03}_{-0.02}$	3.55e + 52
$14.50 \sim 15.00$	$6.68\sim6.91$	80.00	$-1.01^{+0.04}_{-0.04}$	$648.6^{+79.1}_{-80.5}$	$22.8^{+2.2}_{-2.2}$	-41.5	$0.75^{+0.51}_{-0.30}$	$15.08^{+3.14}_{-2.32}$	$0.05^{+0.04}_{-0.02}$	2.82e + 52
$15.00 \sim 15.50$	$6.91 \sim 7.14$	87.43	$-0.92^{+0.04}_{-0.04}$	$494.1^{+51.9}_{-50.7}$	$23.7^{+1.9}_{-1.9}$	-50.0	$0.96^{+0.54}_{-0.33}$	$15.80^{+3.08}_{-2.56}$	$0.06^{+0.04}_{-0.02}$	2.96e + 52
$15.50 \sim 16.00$	$7.14 \sim 7.37$	91.73	$-0.95^{+0.04}_{-0.04}$	$582.5^{+63.7}_{-65.1}$	$24.0^{+1.6}_{-1.6}$	-80.8	$1.30^{+0.56}_{-0.39}$	$17.48^{+3.38}_{-2.64}$	$0.07^{+0.03}_{-0.02}$	3.27e + 52
$16.00\sim16.50$	$7.37 \sim 7.60$	90.06	$-1.02^{+0.04}_{-0.04}$	$640.4^{+91.4}_{-92.2}$	$25.6^{+2.2}_{-2.2}$	-51.2	$1.10^{+0.58}_{-0.41}$	$16.62^{+3.91}_{-2.84}$	$0.07^{+0.04}_{-0.03}$	3.11e+52
$16.50\sim17.00$	$7.60\sim7.83$	90.67	$-0.96^{+0.04}_{-0.04}$	$576.5^{+78.4}_{-77.9}$	$30.3^{+5.5}_{-5.2}$	-25.1	$0.71^{+0.87}_{-0.48}$	$18.83^{+4.75}_{-3.42}$	$0.04^{+0.05}_{-0.03}$	3.53e + 52
$17.00\sim17.50$	$7.83 \sim 8.06$	97.88	$-0.92^{+0.04}_{-0.04}$	$561.8_{-63.6}^{+62.8}$	$26.8^{+2.8}_{-2.8}$	-40.2	$1.03^{+0.72}_{-0.42}$	$20.40^{+3.97}_{-3.30}$	$0.05^{+0.04}_{-0.02}$	3.82e + 52
$17.50\sim18.00$	$8.06 \sim 8.29$	82.94	$-1.13^{+0.03}_{-0.03}$	$2375.2^{+440.5}_{-440.1}$	$33.8^{+3.1}_{-3.2}$	-68.8	$1.35^{+0.83}_{-0.55}$	$31.18^{+7.03}_{-5.27}$	$0.04^{+0.03}_{-0.02}$	5.84e + 52
$18.00\sim18.50$	$8.29 \sim 8.53$	77.25	$-1.17\substack{+0.04 \\ -0.04}$	$2143.3_{-532.9}^{+521.4}$	$32.5^{+2.5}_{-2.5}$	-65.0	$1.37^{+0.74}_{-0.45}$	$23.06^{+6.84}_{-4.79}$	$0.06^{+0.04}_{-0.02}$	4.32e + 52

Note. The definitions of parameters are the same as in Table 2.

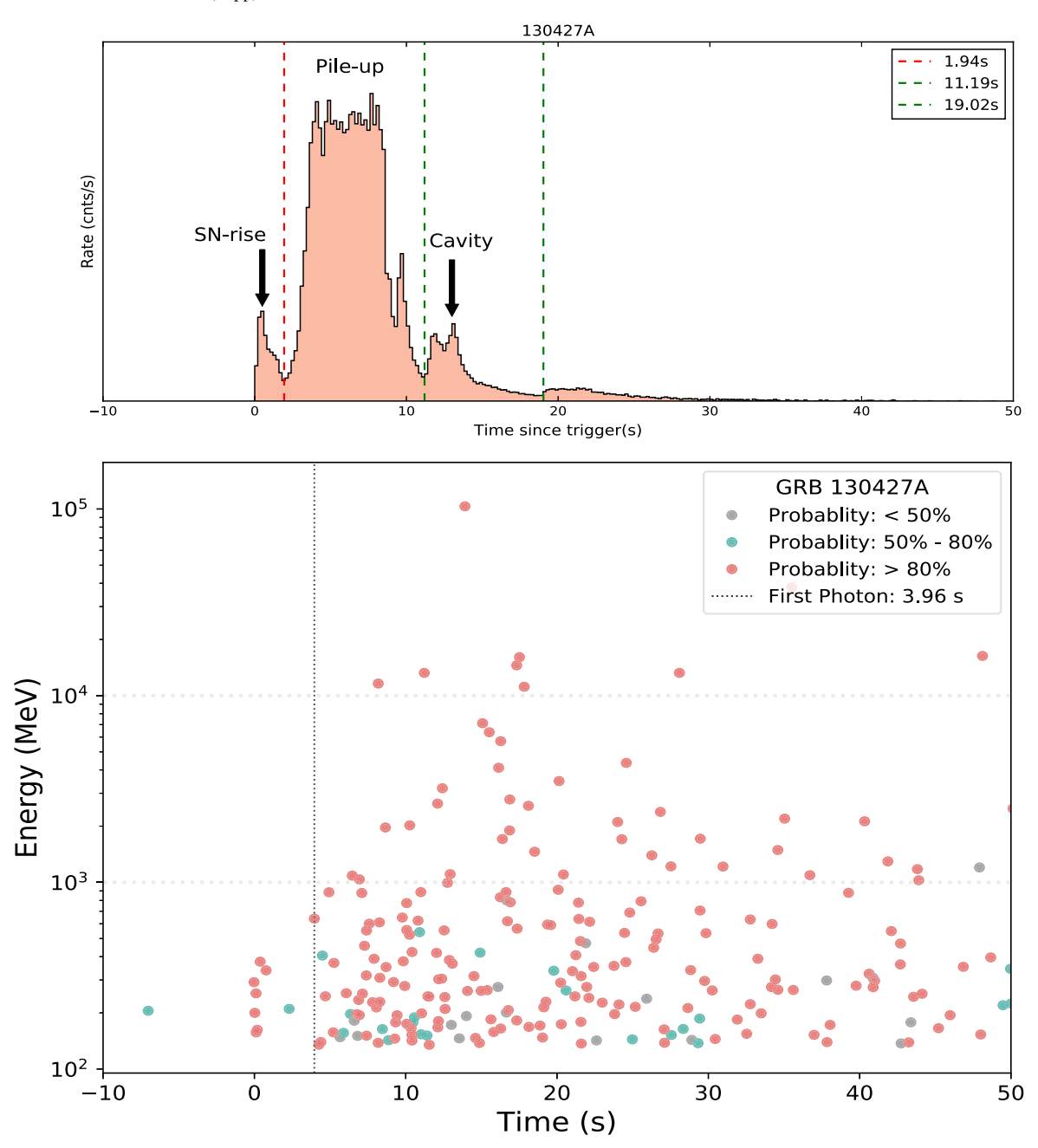


Figure 10. Upper panel: time structure of the prompt emission phase of GRB 130427A presented in the rest frame. The Fermi-GBM observation is strongly piled up due to the high fluence, hence the detection of each episode, especially the starting time of the UPE phase, cannot be determined accurately. Lower panel: the energy and time of each Fermi-LAT photon in the rest-frame; the first photon of GeV energy occurs at $t_{\rm rf} = 3.96$ s. The onset of the GeV radiation coincides with the onset of the UPE. For detailed information for each episode (SN-rise, cavity, GeV, and afterglow), see Section 5 and Table 5, which includes the starting time, the duration, the isotropic energy, and the preferred model.

Episode	Starting Time Rest-frame	Ending Time Rest-frame	Energy (erg)	Spectrum	References
SN-rise	0 s	0.49 s	6.5×10^{51}	CPL + BB	New in this paper
UPE	1.94 s	11.19 s	$\sim 1.4 \times 10^{54}$	CPL + BB	New in this paper
Cavity	11.19 s	19.03 s	1.97×10^{52}	CPL	New in this paper
GeV	3.96 s	$> 2 \times 10^4 \text{ s}$	5.69×10^{52}	PL	Ruffini et al. (2015)
Afterglow	107 s	>10 days	2.65×10^{52}	PL	Ruffini et al. (2015)

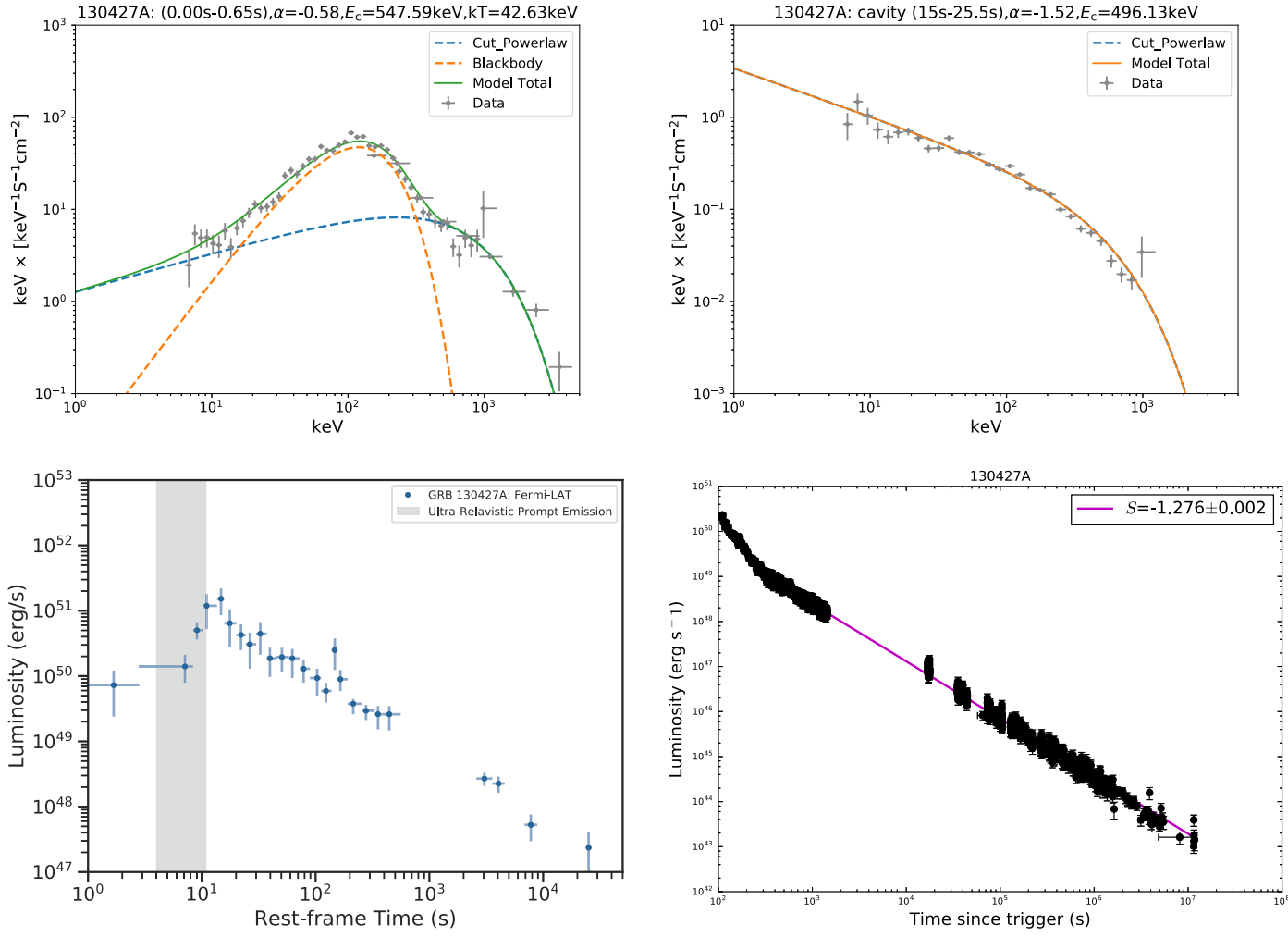


Figure 11. SN-rise, cavity, GeV, and afterglow of GRB 130427A; see also Table 5, which includes, for each episode, the starting time, the duration, the isotropic energy, and the model that best fits the spectrum. Upper left: SN-rise spectrum, well fitted by a CPL + BB model, from 0 to 0.65 s ($t_{\rm rf} \simeq 0.49$ s); the spectral index α is -0.58, cutoff energy $E_{\rm c}$ is 547.59 keV, and the BB temperature is 42.63 keV in the observer's frame. The detailed information of the properties of the SN-rise in BdHNe I for the case can be found in Section 5 and in Table 7, which includes the duration in both the rest frame and observer's frame, the energy flux, the energy of SN-rise, the total energy, the blackbody temperature, and the redshift. Upper right: featureless spectrum of the cavity emission from ≈ 15 s ($t_{\rm rf} = 11.19$ s) to ≈ 25.5 s ($t_{\rm rf} = 19.03$ s) fitted by a CPL, where the photon index α is -1.52 and the cutoff energy is 496.13 keV in the observer's frame. For detailed information on each episode (SN-rise, cavity, GeV, and afterglow), see Section 5 and Table 5, which includes the starting time, the duration, the isotropic energy, and the preferred model. Lower left: Fermi-LAT rest-frame light curve in the 100 MeV-100 GeV energy range. The UPE region is shaded gray. Lower right: k-corrected X-ray afterglow luminosity observed by Swift-XRT in the 0.3–10 keV energy range, as a function of the rest-frame time. It is best fitted by a power law with index 1.276 \pm 0.002.

8. Conclusions

In this paper, we have selected for this extended analysis three BdHNe I, GRB 160625B, GRB 160509A, and GRB 130427A, as well as BdHN II GRB 180728A, aiming to identify and verify the BdHNe I properties in these three additional sources, and compare and contrast the results with those of the BdHN II (Wang et al. 2019b). In GRB 160509A and GRB 160625B, we have first identified the aforementioned three BdHN I episodes. In the UPE phase, we have performed a time-resolved spectral analysis following the iterative process in a sequence of ever decreasing time intervals. We have also examined both the GeV radiation and the afterglow following the UPE phase. The same procedure has been repeated in the case of GRB 130427A with the exception of the UPE phase in view of a pileup problem. The case of GRB 180728A, a BdHN II, has been used as a counterexample. For GRB 160509A and GRB 160625B, we have also performed a time-resolved analysis on an iterative process in a sequence of ever decreasing time intervals: this has allowed us to find the self-similar structures and identify as well the associated power laws in the UPE phase. We have also identified in all four sources, following the analysis of GRB 130427A in the companion paper (Ruffini et al. 2019d), the GeV radiation during and following the UPE phase as well as in the afterglow emission. Also in all the four sources, we describe the spectral properties of their afterglow emission, including the mass estimate of the ν NS, following the results presented in the companion paper (Rueda et al. 2020).

The unprecedented vast spectral analysis, iterative in ever decreasing time steps, has successfully led to confirmation of the self-similarities and power laws, discovered initially in GRB 190114C, as a common feature of the UPE of BdHNe I. The results of the spectral analysis of GRB 190114C have been confirmed and have validated the common properties in all BdHNe I: the three episodes as well as the self-similar structures and the associated power laws in the UPE phase. The profound similarities of the results have made a significant step

 Table 6

 Episodes of GRB 180728A with the Parameters Defined as in Table 1 Except This GRB as a BdHN II has no GeV Emission

Episode	Starting Time Rest-frame	Ending Time Rest-frame	Energy (erg)	Spectrum	References
SN-rise	0 s	2.46 s	7.98×10^{49}	PL	Wang et al. (2019b)
Prompt emission	7.81 s	11.82 s	2.73×10^{51}	CPL + BB	Wang et al. (2019b)
Cavity					Wang et al. (2019b)
GeV					Wang et al. (2019b)
Afterglow	1556 s	>10 days	5.81×10^{50}	PL	Wang et al. (2019b)

Note. Prompt emission is without self-similarity.

Table 7Properties of the SN-rise in BdHNe I: GRB 190114C, GRB 130427A, GRB 160509A, and GRB 160625B; and in a BdHN II: GRB 180728A

GRB	$t_1 \sim t_2$ (s)	Duration (s)	Flux (erg cm ⁻² s ⁻¹)	$E_{ m sh}$ (erg)	$E_{\rm iso}$ (erg)	Temperature (keV)	Redshift	References
	(Observation)	(Rest)	,	(SN-rise)	(Total)	(Rest)		(For SN-rise)
190114C	1.12 ~ 1.68	0.39	$1.06^{+0.20}_{-0.20} \times 10^{-4}$	$2.82^{+0.13}_{-0.13} \times 10^{52}$	$(2.48 \pm 0.20) \times 10^{53}$	$27.4_{-25.6}^{+45.4}$	0.424	Melandri et al. (2019)
130427A	$0.0 \sim 0.65$	0.49	$2.14^{+0.28}_{-0.26} \times 10^{-5}$	$650^{+1.70}_{-1.70} \times 10^{51}$	$\sim 1.40 \times 10^{54}$	44.9+1.5	0.3399	Xu et al. (2013a)
160509A	$2.0 \sim 4.0$	0.92	$1.82^{+1.23}_{-0.76} \times 10^{-6}$	$1.47^{+0.60}_{-0.60} \times 10^{52}$	$\sim 1.06 \times 10^{54}$	$25.6^{+4.8}_{-4.7}$	1.17	Tam et al. (2017)
160625B	$0\sim 2.0$	0.83	$6.8^{+1.6}_{-1.6} \times 10^{-7}$	$1.09^{+0.20}_{-0.20} \times 10^{52}$	$\sim 3.00 \times 10^{54}$	$36.8^{+1.9}_{-1.9}$	1.406	This paper
180728A	$-1.57 \sim 1.18$	0.83	$4.82^{+1.16}_{-0.82} \times 10^{-8}$	$7.98^{+1.92}_{-1.34}\times10^{-3}$	$2.76^{+0.11}_{-0.10}\times10^{51}$	•••	0.117	Izzo et al. (2018)

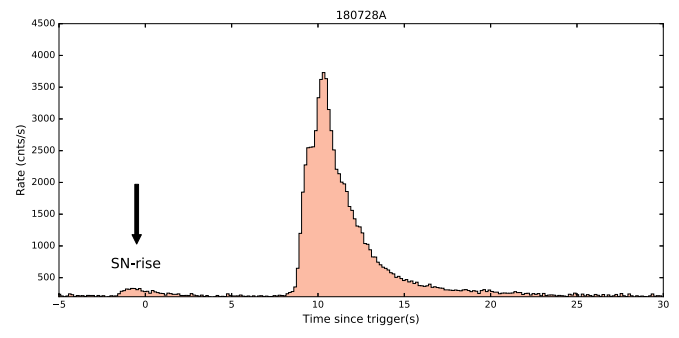


Figure 12. We identify the SN-rise from the CO_{core} of a BdHN II in GRB 180728A (Wang et al. 2019b). This GRB is composed of two spikes. The first spike, the precursor, shows a power-law spectrum with a power-law index of -2.31 ± 0.08 in its 2.75 s duration. The averaged luminosity is $3.24^{+0.78}_{-0.55} \times 10^{49}$ erg s⁻¹, and the integrated energy gives $7.98^{+1.92}_{-1.34} \times 10^{49}$ erg in the range from 1 keV to 10 MeV. This energy emitted is in agreement with the conversion of the kinetic energy of the SN-rise into electromagnetic emission. We consider the second pulse (prompt emission without selfsimilarity) as due to the hypercritical accretion of the SN ejecta onto the companion NS, starting from 8.72 s and lasting 13.82 s. This pulse contains 2.73×10^{51} erg isotropic energy. The best fit is a CPL + BB model of temperature \approx 7 keV in the observer's frame. The BB component is interpreted as a matter outflow driven by the Rayleigh-Taylor convective instability developed in the accretion process. From the time between observation of the SN-rise and the starting time of the hypercritical accretion, $\Delta t \approx 10$ s, a binary separation of $\approx 3 \times 10^{10}$ cm has been inferred. From the binary separation, by angular momentum conservation, it has been inferred that the spin period of the ν NS left from the collapse of the CO_{core} is \approx 2.5 ms (Wang et al. 2019b). This ν NS powers the afterglow by dissipating its rotational energy.

forward in the taxonomy of GRBs and in evidencing a standard composition of BdHNe I. This opens the opportunity of a wider inquiry into the astrophysical nature of their components in the population synthesis approach: e.g., the BH formation in all BdHNe I occurs due to accretion of the SN ejecta in a tight binary system with a neutron star companion that reaches its critical mass, leading to the formation of the BH. The SN-rises

in all five BdHNe are compared and contrasted. The most farreaching discovery of self-similarities and power laws (see also Ruffini et al. 2019a, 2019d), confirmed extensively here, leads to the existence of a discrete quantized repetitive polarized emission, in both the GeV and MeV energies observed by Fermi-GBM and Fermi-LAT, on a timescale as short as 10^{-14} s. These results open new paths in the discovery of fundamental physical laws.

In Ruffini et al. (2019a), we have introduced a novel time-resolved spectral analysis technique, adopting ever decreasing time steps, in the analysis of GRB 190114C. This has led to the discovery of the three episodes and the self-similarity and power laws in BdHNe I. In this paper, we have made a major effort in applying such a time-resolved spectral analysis to BdHNe I: GRB 130427A, GRB 160509A, and GRB 160625B. We have proved that, indeed, all the results obtained in GRB 190114C, far from making it an exception, do characterize the physics of BdHNe I. This opens as well a new direction of research, that is to insert in population synthesis analyses the nature of every single component of a BdHN. At the same time, there is the urgency of understanding the physical origin of the self-similarity and power laws, which has been addressed for the first time in the companion paper (Ruffini et al. 2019d).

These results open new perspective of research: (1) to study the new physical process characterizing each single episode of a BdHN in the context of previously unexplored regimes: e.g., the analysis of the SN not following the traditional description as an isolated system and identifying their properties within a BdHN I, and alternatively in a BdHN II; (2) to insert the BdHN evolution in the framework of a population synthesis analysis; (3) to address the new physical process underlying the existence of the observed self-similarities and power laws, which reveals a discrete sequence of quantized events with quanta of 10³⁷ erg on new timescales of 10⁻¹⁴ s (see Ruffini et al. 2019d; Rueda & Ruffini 2020), and to explore the new

directions open to the identification of fundamental new laws of our universe.

In the BdHN model, the BH inner engine starts to act once it forms: it accelerates charged particles, which meanwhile radiate photons in a wide energy band, generating the UPE phase and the GeV light curve. The UPE phase is signified by the thermal components since the original plasma is optically thick. As we have observed in the above BdHNe I, the starting time of thermal emission is very close to the observational time of the first GeV photon, with a discrepancy of at most a fraction of a second. Considering that the initial count rate of GeV photons reaches only a few photons per second, it is reasonable to assume that the thermal emission coincides with the GeV emission from the observation.

Since we have now shown that BdHNe I are standard, we compare and contrast their SN-rise with one example of a BdHN II and with the case of SN shockwave breakout in GRB 060218 as an example of how it is not possible to speak of a SN out of context of its evolution as one example of this new astrophysics.

We thank the anonymous referee for his/her valuable comments and suggestions. Some important points of this work were performed during the authors' visit to University of Science and Technology of China, Hefei.

ORCID iDs

```
Liang Li  https://orcid.org/0000-0002-1343-3089

R. Moradi  https://orcid.org/0000-0002-2516-5894

R. Ruffini  https://orcid.org/0000-0003-0829-8318
```

References

```
Abdo, A. A., Ackermann, M., Ajello, M., et al. 2010, ApJ, 712, 558
Abdo, A. A., Ackermann, M., Arimoto, M., et al. 2009, Sci, 323, 1688
Ackermann, M., Ajello, M., Asano, K., et al. 2013, ApJS, 209, 11
Ackermann, M., Ajello, M., Asano, K., et al. 2014, Sci, 343, 42
Ajello, M., Arimoto, M., Axelsson, M., et al. 2019, ApJ, 878, 52
Arnett, W. D. 1982, ApJ, 253, 785
Band, D., Matteson, J., Ford, L., et al. 1993, ApJ, 413, 281
Becerra, L., Bianco, C. L., Fryer, C. L., Rueda, J. A., & Ruffini, R. 2016, ApJ,
  833, 107
Becerra, L., Cipolletta, F., Fryer, C. L., Rueda, J. A., & Ruffini, R. 2015, ApJ,
   812, 100
Becerra, L., Ellinger, C. L., Fryer, C. L., Rueda, J. A., & Ruffini, R. 2019, ApJ,
Becerra, L., Guzzo, M. M., Rossi-Torres, F., et al. 2018, ApJ, 852, 120
Bennett, C. L., Larson, D., Weiland, J. L., & Hinshaw, G. 2014, ApJ, 794, 135
Bethe, H. A. 1990, RvMP, 62, 801
Bhat, P. N., Meegan, C. A., von Kienlin, A., et al. 2016, ApJS, 223, 28
Burns, E. 2016, GCN, 19581, 1
Campana, S., Mangano, V., Blustin, A. J., et al. 2006, Natur, 442, 1008
Cash, W. 1979, ApJ, 228, 939
Chandrasekhar, S. 1969, Ellipsoidal Figures of Equilibrium (New Haven, CT:
   Yale Univ. Press)
Dirirsa, F., Vianello, G., Racusin, J., & Axelsson, M. 2016, GCN, 19586, 1
Eggleton, P. P. 1983, ApJ, 268, 368
Ferrero, P., Kann, D. A., Zeh, A., et al. 2006, A&A, 457, 857
Flores, H., Covino, S., Xu, D., et al. 2013, GCN, 14491, 1
Fryer, C. L., Oliveira, F. G., Rueda, J. A., & Ruffini, R. 2015, PhRvL, 115,
Fryer, C. L., Rueda, J. A., & Ruffini, R. 2014, ApJL, 793, L36
Fujisawa, K., Okawa, H., Yamamoto, Y., & Yamada, S. 2019, ApJ, 872, 155
Gilkis, A. 2018, MNRAS, 474, 2419
Goldstein, A., Burgess, J. M., Preece, R. D., et al. 2012, ApJS, 199, 19
Gruber, D., Goldstein, A., von Ahlefeld, V. W., et al. 2014, ApJS, 211, 12
Guiriec, S., Briggs, M. S., Connaugthon, V., et al. 2010, ApJ, 725, 225
Guiriec, S., Connaughton, V., Briggs, M. S., et al. 2011, ApJL, 727, L33
Guiriec, S., Daigne, F., Hascoët, R., et al. 2013, ApJ, 770, 32
```

```
Guiriec, S., Kouveliotou, C., Daigne, F., et al. 2015a, ApJ, 807, 148
Guiriec, S., Mochkovitch, R., Piran, T., et al. 2015b, ApJ, 814, 10
Hamburg, R., Veres, P., Meegan, C., et al. 2019, GCN, 23707, 1
Hurley, J. R., Tout, C. A., & Pols, O. R. 2002, MNRAS, 329, 897
Izzo, L., Rossi, A., Malesani, D. B., et al. 2018, GCN, 23142, 1
Izzo, L., Rueda, J. A., & Ruffini, R. 2012, A&A, 548, L5
Kaneko, Y., Preece, R. D., Briggs, M. S., et al. 2006, ApJS, 166, 298
Kangas, T., Fruchter, A. S., Cenko, S. B., et al. 2020, ApJ, 894, 43
Laskar, T., Alexander, K. D., Berger, E., et al. 2016, ApJ, 833, 88
Levan, A. J., Cenko, S. B., Perley, D. A., & Tanvir, N. R. 2013, GCN, 14455, 1
Li, L. 2019a, ApJS, 242, 16
Li, L. 2019b, ApJS, 245, 7
Li, L. 2020, ApJ, 894, 100
Li, L. 2022a, ApJ, 941, 27
Li, L. 2022b, arXiv:2211.12187
Li, L., Geng, J.-J., Meng, Y.-Z., et al. 2019, ApJ, 884, 109
Li, L., Ryde, F., Pe'er, A., Yu, H.-F., & Acuner, Z. 2021, ApJS, 254, 35
Li, L., & Zhang, B. 2021, ApJS, 253, 43
Longo, F., Bissaldi, E., Bregeon, J., et al. 2016, GCN, 19403, 1
Lü, H.-J., Lü, J., Zhong, S.-Q., et al. 2017, ApJ, 849, 71
Lu, R.-J., Wei, J.-J., Liang, E.-W., et al. 2012, ApJ, 756, 112
Maselli, A., Beardmore, A. P., Lien, A. Y., et al. 2013, GCN, 14448, 1
Maselli, A., Melandri, A., Nava, L., et al. 2014, Sci, 343, 48
Meegan, C., Lichti, G., Bhat, P. N., et al. 2009, ApJ, 702, 791
Melandri, A., D'Avanzo, P., D'Elia, V., et al. 2016, GCN, 19585, 1
Melandri, A., Izzo, L., D'Avanzo, P., et al. 2019, GCN, 23983, 1
Mirabal, N., Halpern, J. P., An, D., Thorstensen, J. R., & Terndrup, D. M.
   2006, ApJL, 643, L99
Mirzoyan, R., Noda, K., Moretti, E., et al. 2019, GCN, 23701, 1
Moradi, R., Rueda, J. A., Ruffini, R., et al. 2021, PhRvD, 104, 063043
Moreno, E., Vazquez-Polo, F. J., & Robert, C. P. 2013, arXiv:1310.2905
Nakamura, K., Kuroda, T., Takiwaki, T., & Kotake, K. 2014, ApJ, 793, 45
Perri, M., Evans, P. A., Osborne, J. P., et al. 2018, GCN, 23049, 1
Pian, E., Mazzali, P. A., Masetti, N., et al. 2006, Natur, 442, 1011
Planck Collaboration, Ade, P. A. R., Aghanim, N., et al. 2016, A&A, 594, A13
Preece, R. D., Briggs, M. S., Mallozzi, R. S., et al. 2000, ApJS, 126, 19
Ravasio, M. E., Ghirlanda, G., Nava, L., & Ghisellini, G. 2019, A&A,
  625, A60
Rossi, R., Izzo, L., Milvang-Jensen, B., et al. 2018, GCN, 23055, 1
Rueda, J. A., & Ruffini, R. 2020, EPJC, 80, 300
Rueda, J. A., Ruffini, R., Karlica, M., Moradi, R., & Wang, Y. 2020, ApJ,
   893, 148
Rueda, J. A., Ruffini, R., Moradi, R., & Wang, Y. 2021, IJMPD, 30, 2130007
Ruffini, R., Aimuratov, Y., Bianco, C. L., et al. 2018a, GCN, 23066, 1
Ruffini, R., Becerra, L., Bianco, C. L., et al. 2018b, ApJ, 869, 151
Ruffini, R., Karlica, M., Sahakyan, N., et al. 2018c, ApJ, 869, 101
Ruffini, R., Li, L., Moradi, R., et al. 2019a, arXiv:1904.04162
Ruffini, R., Melon Fuksman, J. D., & Vereshchagin, G. V. 2019b, ApJ,
   883, 191
Ruffini, R., Moradi, R., Aimuratov, Y., et al. 2019c, GCN, 23715, 1
Ruffini, R., Moradi, R., Rueda, J. A., et al. 2019d, ApJ, 886, 82
Ruffini, R., Moradi, R., Rueda, J. A., et al. 2021, MNRAS, 504, 5301
Ruffini, R., Muccino, M., Bianco, C. L., et al. 2014, A&A, 565, L10
Ruffini, R., Wang, Y., Aimuratov, Y., et al. 2018d, ApJ, 852, 53
Ruffini, R., Wang, Y., Enderli, M., et al. 2015, ApJ, 798, 10
Ryde, F. 2004, ApJ, 614, 827
Ryde, F. 2005, ApJL, 625, L95
Selsing, J., Izzo, L., Rossi, A., et al. 2018, GCN, 23181, 1
Selsing, J., Fynbo, J. P. U., Heintz, K. E., & Watson, D. 2019, GCN, 23695, 1
Sollerman, J., Jaunsen, A. O., Fynbo, J. P. U., et al. 2006, A&A, 454, 503
Spiegelhalter, D. J., Best, N. G., Carlin, B. P., & van der Linde, A. 2002, J. R.
                  B, 64, 583
Starling, R. L. C., Barthelmy, S. D., Lien, A. Y., et al. 2018, GCN, 23046, 1
Tak, D., Guiriec, S., Uhm, Z. L., et al. 2019, ApJ, 876, 76
Tam, P.-H.-T., He, X.-B., Tang, Q.-W., & Wang, X.-Y. 2017, ApJL, 844, L7
Tanvir, N. R., Levan, A. J., Cenko, S. B., et al. 2016, GCN, 19419, 1
Troja, E. 2017, AAS/HEAD, 16, 305.05
Troja, E., Lipunov, V. M., Mundell, C. G., et al. 2017, Natur, 547, 425
Veres, P., Meegan, C., & Mailyan, B. 2018, GCN, 23053, 1
Vianello, G., Lauer, R. J., Younk, P., et al. 2015, arXiv:1507.08343
von Kienlin, A. 2013, GCN, 14473, 1
von Kienlin, A., Meegan, C. A., Paciesas, W. S., et al. 2014, ApJS, 211, 13
Wang, Y., Li, L., Moradi, R., & Ruffini, R. 2019a, arXiv:1901.07505
Wang, Y., Rueda, J. A., Ruffini, R., et al. 2019b, ApJ, 874, 39
Waxman, E., & Katz, B. 2017, in Handbook of Supernovae, ed.
   A. W. Alsabti & P. Murdin (Cham: Springer), 967
```

Xu, D., Malesani, D., Fynbo, J. P. U., et al. 2016, GCN, 19600, 1

Weinberg, S. 1972, Gravitation and Cosmology: Principles and Applications of the General Theory of Relativity (New York: Wiley-VCH), 688
Woosley, S. E., & Bloom, J. S. 2006, ARA&A, 44, 507
Xu, D., de Ugarte Postigo, A., Leloudas, G., et al. 2013a, ApJ, 776, 98
Xu, D., de Ugarte Postigo, A., Schulze, S., et al. 2013b, GCN, 14478, 1

Yu, H.-F., Dereli-Bégué, H., & Ryde, F. 2019, ApJ, 886, 20
Yu, H.-F., Preece, R. D., Greiner, J., et al. 2016, A&A, 588, A135
Zhang, B. 2018, The Physics of Gamma-Ray Bursts (Cambridge: Cambridge Univ. Press)

Zhang, B.-B., Zhang, B., Castro-Tirado, A. J., et al. 2018, NatAs, 2, 69 Zhang, B.-B., Zhang, B., Liang, E.-W., et al. 2011, ApJ, 730, 141